Finite-strain formulation and FE implementation of a constitutive model for powder compaction*

S. Stupkiewicz[a,b,†], A. Piccolroaz[b], D. Bigoni[b]

[a] Institute of Fundamental Technological Research (IPPT), Pawińskiego 5b, 02-106 Warsaw, Poland

[b] University of Trento, via Mesiano 77, I-38123 Trento, Italy

e-mail: sstupkie@ippt.pan.pl; roaz@ing.unitn.it; bigoni@ing.unitn.it

Abstract

A finite-strain formulation is developed, implemented and tested for a constitutive model capable of describing the transition from granular to fully dense state during cold forming of ceramic powder. This constitutive model (as well as many others employed for geomaterials) embodies a number of features, such as pressure-sensitive yielding, complex hardening rules and elastoplastic coupling, posing considerable problems in a finite-strain formulation and numerical implementation. A number of strategies are proposed to overcome the related problems, in particular, a neo-Hookean type of modification to the elastic potential and the adoption of the second Piola-Kirchhoff stress referred to the intermediate configuration to describe yielding. An incremental scheme compatible with the formulation for elastoplastic coupling at finite strain is also developed, and the corresponding constitutive update problem is solved by applying a return mapping algorithm.

Keywords: plasticity; elastoplastic coupling; finite element method; automatic differentiation

1 Introduction

The formulation and implementation of elastoplastic constitutive equations for metals at large strain have been thoroughly analyzed in the last thirty years, see for instance [1, 2], so that nowadays they follow accepted strategies. For these materials, pressure-insensitive yielding, J_3-independence, and incompressibility of plastic flow strongly simplify the mechanical behaviour, while frictional-cohesive and rock-like materials (such as granular media, soils, concretes, rocks, ceramics and powders) are characterized by pressure-sensitive, J_3-dependent yielding, dilatant/contractant flow, nonlinear elastic behaviour even at small strain and elastoplastic coupling. There have been several attempts to generalize treatment of metal plasticity at large strain in this context [3, 4, 5, 6, 7, 8, 9], but many

*Published in *Comput. Meth. Appl. Mech. Engrg.* 283:856–880, 2015, doi:10.1016/j.cma.2014.09.027

†Corresponding author

problems still remain not completely solved. These include the form of the elastic potential, the stress measure to be employed in the yield function, which has to provide an easy interpretation of experiments, the flow rule and the elastic-plastic coupling laws.

The main difficulty in the practical application of finite-strain elastoplasticity models, as opposed to their small-strain counterparts, is related to development and implementation of incremental (i.e., finite-step) constitutive relationships. The difficulties lie, for instance, in formulation and solution of the highly nonlinear constitutive update problem, consistent treatment of plastic incompressibility (or plastic volume changes), and consistent linearization of the incremental relationships. The last issue is of the utmost importance for overall computational efficiency of the finite element models because consistent linearization (consistent tangent) is needed to achieve the quadratic convergence of the Newton method.

In the present paper, the model for cold forming of ceramic powders proposed by Piccolroaz et al. [10, 11] (called 'PBG model' in the following) is developed for large strain analyses, implemented in the finite element method and numerically tested. The need for this large-strain generalization is related to the fact that during ceramic forming the mean strain can easily reach 50%, while peaks can touch 80%. The differences between a small strain and a large strain analysis can be appreciated from Figs. 3 and 6 in Section 5.1, where small-strain and large-strain predictions are reported for the force–displacement relation at the top of a rigid mould containing an alumina ceramic powder. Results (pertaining to a flat punch and to a punch with a 'cross-shaped' groove, respectively reported in Fig. 3 and 6) clearly show that the large-strain analyses are more consistent and in closer agreement with experimental results than the analyses performed under the small strain hypothesis.

The model for powder compaction can be considered as paradigmatic of the difficulties that can be encountered in the implementation of models for geomaterials, since many 'unconventional' features of plasticity are simultaneously present to describe the complex transition from a loose granular material (the powder) to a fully dense ceramic (the green body). These difficulties enclose: (i.) the pressure-sensitive, J_3-dependent yield function introduced by Bigoni and Piccolroaz [12] ('BP yield function' in the following), which is defined $+\infty$ in some regions outside the elastic domain; (ii.) a nonlinear elastic behaviour even at small strain, (iii.) changes in elastic response coupled to plastic deformation (elastoplastic coupling).

In this work, incremental (finite-step) constitutive equations are developed and implemented for the finite-deformation version of the PBG model. In order to improve the computational efficiency, the original model [11] is slightly modified, but its essential features, including the elastoplastic coupling, are preserved. Note that a consistent finite-element implementation of the present specific form of elastoplastic coupling at finite strain has not been reported in the literature so far. The model is applied to simulate ceramic powder compaction with account for frictional contact interaction.

The above-mentioned implementation difficulties are efficiently handled by using an advanced hybrid symbolic-numeric approach implemented in *AceGen*, a symbolic code generation system [13, 14]. *AceGen* combines symbolic and algebraic capabilities of *Mathematica*, automatic differentiation (AD) technique, simultaneous optimization of expressions and automatic generation of computer codes, and it is an efficient tool for rapid prototyping of numerical procedures as well as for generation of highly optimized compiled codes (such as finite element subroutines). Finite element computations have been

carried out using *AceFEM*, a highly flexible finite element code that is closely integrated with *AceGen*.

Selected results of 2D and 3D simulations of powder compaction processes have already been reported in [15], and the model predictions have been compared to experimental data showing satisfactory agreement. However, the finite-strain formulation and the numerical strategies adopted for its implementation have not been presented in [15], as that paper was aimed at providing an overview of elastoplastic coupling in powder compaction processes. In the present paper, we provide the details of the formulation and implementation, and we illustrate the ability of the model to properly describe uniform and nonuniform compaction of alumina powder. As an application, we study the effect of friction and initial aspect ratio on compaction of alumina powder in a cylindrical die.

2 PBG model at small strain

The small-strain PBG model [10] is briefly described below as a reference for its finite-strain version introduced in the next section, with a slight modification to the notation to make it more convenient for the subsequent extension to the finite-strain framework. The model is fully defined by specifying the free energy, the yield condition, and the plastic flow rule, and these are provided below. For the details, including justification of the specific constitutive assumptions and calibration of the model for alumina powder, refer to Piccolroaz et al. [10].

2.1 Free energy

The total strain $\boldsymbol{\varepsilon}$ is decomposed into the elastic $\boldsymbol{\varepsilon}_e$ and plastic $\boldsymbol{\varepsilon}_p$ parts,

$$\boldsymbol{\varepsilon} = \boldsymbol{\varepsilon}_e + \boldsymbol{\varepsilon}_p, \tag{1}$$

and the free energy is assumed in the following form,

$$\phi(\boldsymbol{\varepsilon}, \boldsymbol{\varepsilon}_p, p_c) = c\ \mathrm{tr}\,\boldsymbol{\varepsilon}_e + (p_0+c)\left[\left(d-\frac{1}{d}\right)\frac{(\mathrm{tr}\,\boldsymbol{\varepsilon}_e)^2}{2\tilde{\kappa}} + d^{1/n}\tilde{\kappa}\exp\left(-\frac{\mathrm{tr}\,\boldsymbol{\varepsilon}_e}{d^{1/n}\tilde{\kappa}}\right)\right] + \mu\,\mathrm{tr}\,\boldsymbol{\varepsilon}_e^2 - \frac{\mu}{3}(\mathrm{tr}\,\boldsymbol{\varepsilon}_e)^2, \tag{2}$$

where the plastic strain $\boldsymbol{\varepsilon}_p$ and the forming pressure p_c are adopted as internal variables, and $\boldsymbol{\varepsilon}_e = \boldsymbol{\varepsilon} - \boldsymbol{\varepsilon}_p$. Note that the free energy (2) is a convex function of $\boldsymbol{\varepsilon}_e$. The *elastoplastic coupling* is here introduced through the dependence of cohesion c, parameter d and shear modulus μ on the forming pressure p_c, namely

$$c = c_\infty[1 - \exp(-\Gamma\langle p_c - p_{cb}\rangle)], \tag{3}$$

$$d = 1 + B\langle p_c - p_{cb}\rangle, \tag{4}$$

$$\mu = \mu_0 + c\left(d - \frac{1}{d}\right)\mu_1, \tag{5}$$

where $\langle\cdot\rangle$ denotes the Macauley brackets operator, $\tilde{\kappa} = \kappa/(1+e_0)$ and κ, e_0, p_0, n, c_∞, Γ, p_{cb}, B, μ_0 and μ_1 are material parameters. Note that the elastoplastic coupling is related to the variation in d, so that, if d remains constant and equal to one, the elastic properties of the material remain unchanged during plastic flow.

The forming pressure p_c is assumed to depend on the volumetric part of the plastic strain through the following relationship

$$\operatorname{tr} \boldsymbol{\varepsilon}_p = \mathcal{H}(p_c), \qquad \mathcal{H}(p_c) = -\tilde{a}_1 \exp\left(-\frac{\Lambda_1}{p_c}\right) - \tilde{a}_2 \exp\left(-\frac{\Lambda_2}{p_c}\right), \tag{6}$$

where $\tilde{a}_i$ and Λ_i are material parameters. In view of the above dependence, the free energy could formally be expressed solely in terms of the total strain $\boldsymbol{\varepsilon}$ and the plastic strain $\boldsymbol{\varepsilon}_p$. However, the dependence of p_c on $\boldsymbol{\varepsilon}_p$ is implicit, i.e., p_c cannot be expressed as an explicit function of $\boldsymbol{\varepsilon}_p$. It is thus convenient to keep p_c as an internal variable with the additional constraint introduced by Eq. (6), see Section 4.3.

Note that the forming pressure p_c and the cohesion c are also used to define the yield surface (see below). The corresponding governing equations (6) and (3) are thus called 'hardening laws' in [10].

2.2 Inelastic strain rate

The elastoplastic coupling, introduced above through the dependence of the free energy ϕ on the plastic strain $\boldsymbol{\varepsilon}_p$ and the forming pressure p_c, is a crucial feature of the model. As a result, the stress depends not only on the elastic strain, but also on the internal variables. Indeed, the stress $\boldsymbol{\sigma}$ is defined by

$$\boldsymbol{\sigma} = \frac{\partial \phi}{\partial \boldsymbol{\varepsilon}}, \tag{7}$$

and its rate involves the contributions due to the evolution of the internal variables,

$$\dot{\boldsymbol{\sigma}} = \frac{\partial \boldsymbol{\sigma}}{\partial \boldsymbol{\varepsilon}}[\dot{\boldsymbol{\varepsilon}}] + \frac{\partial \boldsymbol{\sigma}}{\partial \boldsymbol{\varepsilon}_p}[\dot{\boldsymbol{\varepsilon}}_p] + \frac{\partial \boldsymbol{\sigma}}{\partial p_c}\dot{p}_c = \mathbb{E}[\dot{\boldsymbol{\varepsilon}}] + \mathbb{P}[\dot{\boldsymbol{\varepsilon}}_p] + \boldsymbol{P}\dot{p}_c = \mathbb{E}[\dot{\boldsymbol{\varepsilon}} - \dot{\boldsymbol{\varepsilon}}_{in}]. \tag{8}$$

Here, $\mathbb{E}$ is the elastic fourth-order tensor, $\mathbb{P}$ and $\boldsymbol{P}$ describe the elastoplastic coupling, and the inelastic strain rate $\dot{\boldsymbol{\varepsilon}}_{in}$ is defined as

$$\dot{\boldsymbol{\varepsilon}}_{in} = -\mathbb{E}^{-1}\mathbb{P}[\dot{\boldsymbol{\varepsilon}}_p] - \mathbb{E}^{-1}[\boldsymbol{P}\dot{p}_c]. \tag{9}$$

The inelastic strain rate $\dot{\boldsymbol{\varepsilon}}_{in}$ is thus not equal to the plastic strain rate $\dot{\boldsymbol{\varepsilon}}_p$, and the former will be used in the plastic flow rule, which is crucial for a consistent treatment of the elastoplastic coupling, see Bigoni [16]. The model is rate-independent, hence by the time we understand here a time-like load parameter.

2.3 Yield condition

The yield condition is defined using the Bigoni–Piccolroaz (BP) yield function [12]

$$F(\boldsymbol{\sigma}, p_c) = f(p, p_c) + \frac{q}{g(\theta)} \leq 0, \tag{10}$$

where

$$f(p, p_c) = \begin{cases} -M p_c \sqrt{(\Phi - \Phi^m)[2(1-\alpha)\Phi + \alpha]} & \text{if } \Phi \in [0,1], \\ +\infty & \text{otherwise,} \end{cases} \qquad \Phi = \frac{p + c}{p_c + c}, \tag{11}$$

$$g(\theta) = \frac{1}{\cos[\beta\pi/6 - (1/3)\cos^{-1}(\gamma\cos 3\theta)]}, \tag{12}$$

and p, q and θ are the usual invariants of the stress tensor,

$$p = -\frac{1}{3}\operatorname{tr}\boldsymbol{\sigma}, \qquad q = \sqrt{3J_2}, \qquad \theta = \frac{1}{3}\cos^{-1}\left(\frac{3\sqrt{3}}{2}\frac{J_3}{J_2^{3/2}}\right), \tag{13}$$

$$J_2 = \frac{1}{2}\operatorname{tr}(\operatorname{dev}\boldsymbol{\sigma})^2, \qquad J_3 = \frac{1}{3}\operatorname{tr}(\operatorname{dev}\boldsymbol{\sigma})^3, \qquad \operatorname{dev}\boldsymbol{\sigma} = \boldsymbol{\sigma} - \frac{1}{3}(\operatorname{tr}\boldsymbol{\sigma})\boldsymbol{I}. \tag{14}$$

The forming pressure p_c and the cohesion c, which depends on p_c through Eq. (3), define the size of the yield surface $F = 0$ and its position along the hydrostatic axis. Parameters M, m, α, β and γ define the shape of the yield surface and are assumed constant.

It is seen from Eq. (11) that the BP yield function F is defined infinity for $p \notin [-c, p_c]$, so it cannot be evaluated numerically for an arbitrary stress state, and incremental schemes employing, for instance, the return mapping algorithm cannot be applied directly. Therefore, following Stupkiewicz et al. [17], an alternative implicit yield function F^* is used in practice, which has the same zero level set $F^* = 0$ as the original yield function (i.e., $F = 0$) but behaves well for arbitrary stress states, see Section 4.1.

2.4 Plastic flow rule

The flow rule is expressed in terms of the inelastic strain rate $\dot{\boldsymbol{\varepsilon}}_{in}$ rather than the plastic strain rate $\dot{\boldsymbol{\varepsilon}}_p$, see Bigoni [16],

$$\dot{\boldsymbol{\varepsilon}}_{in} = \dot{\lambda}\hat{\boldsymbol{n}}, \qquad \hat{\boldsymbol{n}} = \boldsymbol{n} - \frac{1}{3}\epsilon(1-\Phi)(\operatorname{tr}\boldsymbol{n})\boldsymbol{I}, \qquad \boldsymbol{n} = \frac{\partial F}{\partial \boldsymbol{\sigma}}, \tag{15}$$

where $\dot{\lambda}$ is the plastic multiplier satisfying the usual complementarity conditions,

$$\dot{\lambda} \geq 0, \qquad F \leq 0, \qquad \dot{\lambda}F = 0. \tag{16}$$

Here, ϵ is a parameter that governs non-associativity of the flow rule ($0 \leq \epsilon < 1$), and $\epsilon = 0$ corresponds to the associated flow rule.

3 PBG model at finite strain

The PBG model [10] has been extended to the finite-strain framework by the same group of authors in [11]. In that model, the usual multiplicative decomposition of the deformation gradient has been adopted, the free energy has been expressed in terms of the logarithmic elastic strain while keeping the same form (2) of the free energy function, and the BP yield condition has been expressed in terms of the Biot stress tensor referred to the initial configuration. With regard to the elastoplastic coupling and plastic flow rule, the Biot stress and its conjugate strain measure have been used to define the inelastic strain rate (using the general framework developed by Bigoni [16]), and that inelastic strain rate has subsequently been used in the plastic flow rule. Finally, a complete set of rate equations has been derived; however, incremental formulation and it finite element implementation have not been attempted.

In this section, a finite-strain formulation of the PBG model is introduced, which is more convenient for the finite-element implementation than the original formulation of Piccolroaz et al. [11]. At the same time, the essential features of that model are preserved, namely the specific form of the free energy function, the elastoplastic coupling framework of Bigoni [16], the BP yield condition [12], and the plastic flow rule. The main difference is in the selection of the internal variables and in the choice of the stress and strain measures used to define the inelastic strain rate and to formulate the flow rule. Also, the yield condition is here expressed in terms of the second Piola-Kirchhoff stress referred to the intermediate configuration rather than in terms of the Biot stress referred to the initial reference configuration which seems more consistent with respect to the experimental testing procedures that are typically used to calibrate the model.

3.1 Free energy

The deformation gradient $\boldsymbol{F}$ is multiplicatively split into elastic $\boldsymbol{F}_e$ and plastic $\boldsymbol{F}_p$ parts,

$$\boldsymbol{F} = \boldsymbol{F}_e \boldsymbol{F}_p, \tag{17}$$

and the following standard kinematic quantities are introduced,

$$\boldsymbol{C} = \boldsymbol{F}^T \boldsymbol{F}, \qquad \boldsymbol{C}_p = \boldsymbol{F}_p^T \boldsymbol{F}_p, \qquad \boldsymbol{b}_e = \boldsymbol{F}_e \boldsymbol{F}_e^T = \boldsymbol{F} \boldsymbol{C}_p^{-1} \boldsymbol{F}^T, \tag{18}$$

respectively, the total and plastic right Cauchy–Green tensors, and the elastic left Cauchy–Green tensor. Furthermore, we have

$$J = J_e J_p, \quad J = \det \boldsymbol{F}, \quad J_e = \det \boldsymbol{F}_e = (\det \boldsymbol{b}_e)^{1/2}, \quad J_p = \det \boldsymbol{F}_p = (\det \boldsymbol{C}_p)^{1/2}. \tag{19}$$

In order to conveniently treat the volumetric strains, which are essential in modeling of powder compaction, the logarithmic elastic and plastic strain tensors are introduced,

$$\boldsymbol{\epsilon}_e = \log \boldsymbol{V}_e = \frac{1}{2} \log \boldsymbol{b}_e, \qquad \boldsymbol{E}_p^{(0)} = \log \boldsymbol{U}_p = \frac{1}{2} \log \boldsymbol{C}_p, \tag{20}$$

where $\boldsymbol{F}_e = \boldsymbol{V}_e \boldsymbol{R}_e$, $\boldsymbol{b}_e = \boldsymbol{V}_e^2$, $\boldsymbol{F}_p = \boldsymbol{R}_p \boldsymbol{U}_p$, and $\boldsymbol{C}_p = \boldsymbol{U}_p^2$. The well-known benefit of using the logarithmic strain measure is that the volumetric strain is simply obtained as a trace of the corresponding strain tensor, and the total volumetric strain is additively decomposed into elastic and plastic contributions.

Following Piccolroaz et al. [11], the free energy can be assumed in the same functional form as in the small-strain model, Eq. (2), with the infinitesimal elastic strain $\boldsymbol{\varepsilon}_e$ simply replaced by the logarithmic strain $\boldsymbol{\epsilon}_e$. However, this form is not efficient in numerical implementation, and a modified free energy function is adopted in this work. For completeness, application of the original free energy of Piccolroaz et al. [11] is discussed in Appendix A.

In the modified free energy function, the volumetric behavior is described in terms of the logarithmic elastic strain $\boldsymbol{\epsilon}_e$, just like in the original model [11], while the shear behavior is described by the term of the neo-Hookean type formulated for the isochoric part of the elastic left Cauchy–Green tensor $\boldsymbol{b}_e$, namely

$$\phi(\boldsymbol{C}, \boldsymbol{C}_p, p_c) = c \ \mathrm{tr}\, \boldsymbol{\epsilon}_e + (p_0 + c) \left[\left(d - \frac{1}{d} \right) \frac{(\mathrm{tr}\, \boldsymbol{\epsilon}_e)^2}{2\tilde{\kappa}} + d^{1/n} \tilde{\kappa} \exp\left(-\frac{\mathrm{tr}\, \boldsymbol{\epsilon}_e}{d^{1/n} \tilde{\kappa}} \right) \right] + \frac{1}{2} \mu (\bar{I}_2 - 3), \tag{21}$$

where

$$\bar{I}_2 = \operatorname{tr} \bar{\boldsymbol{b}}_e = J_e^{-2/3} \operatorname{tr} \boldsymbol{b}_e, \qquad \det \bar{\boldsymbol{b}}_e = 1. \tag{22}$$

The right Cauchy–Green tensor $\boldsymbol{C}$ is adopted as a relevant measure of the total strain in view of the standard objectivity argument, and the plastic right Cauchy–Green tensor $\boldsymbol{C}_p$ is adopted as an internal variable. Since elastic strains are here relatively small, the present modification of the free energy function with respect to that of [11] does not noticeably affect the actual elastic response.

It is shown in Appendix B that the strain energy (21) is a convex function of the variable $\boldsymbol{\epsilon}_e$ and, as a function of $\boldsymbol{F}_e$, it is strongly elliptic, within a range of elastic deformation of interest for a granular material. The former property excludes an unrealistic elastic material softening, while the latter excludes the possibility of an elastic strain localization, which would be unacceptable for a granular material.

The free energy (21) involves two invariants characterizing the elastic strain, $\operatorname{tr} \boldsymbol{\epsilon}_e$ and $\bar{I}_2$, that can be easily expressed in terms of $\boldsymbol{C}$ and $\boldsymbol{C}_p$. Indeed, in view of (18) and (20), we have

$$J_e^2 = (\det \boldsymbol{C})(\det \boldsymbol{C}_p^{-1}), \qquad \operatorname{tr} \boldsymbol{b}_e = \operatorname{tr}(\boldsymbol{C}\boldsymbol{C}_p^{-1}), \tag{23}$$

so that

$$\operatorname{tr} \boldsymbol{\epsilon}_e = \frac{1}{2} \log J_e^2, \qquad \bar{I}_2 = (J_e^2)^{-1/3} \operatorname{tr}(\boldsymbol{C}\boldsymbol{C}_p^{-1}). \tag{24}$$

Parameters c, d and μ in the free energy (21) are assumed to depend on the forming pressure p_c through Eqs. (3)–(5), exactly as in the small-strain model, while the forming pressure p_c is related to $\boldsymbol{C}_p$ by

$$(\det \boldsymbol{C}_p)^{1/2} - 1 = \mathcal{H}(p_c). \tag{25}$$

The above relationship is a consistent generalization of Eq. $(6)_1$ to the finite deformation regime, where function $\mathcal{H}(p_c)$ is specified by Eq. $(6)_2$.

The nonlinear elastic response specified by the free energy function (21) is illustrated in Fig. 1. For volumetric deformation, the mean Cauchy stress $\operatorname{tr} \boldsymbol{\sigma}/3$ is shown in Fig. 1a as a function of the volumetric deformation J_e. In Fig. 1b, the principal Cauchy stress σ_1 is shown as a function of the principal stretch λ_1 for an isochoric deformation defined by $\lambda_2 = \lambda_3 = 1/\lambda_1^{1/2}$. Four values of the forming pressure p_c are considered. In particular, for $p_c = 1$ MPa (smaller than the break-point pressure $p_{cb} = 3.2$ MPa), the material is still a powder with null cohesion ($c = 0$), therefore showing negligible stiffness in tension. By increasing the forming pressure p_c, the material gains cohesion and becomes more and more stiff both in tension and compression. Material parameters correspond to alumina powder and are given in Section 5, Table 1.

3.2 Inelastic strain rate

The inelastic strain rate and subsequently the flow rule are introduced using the Green strain tensor $\boldsymbol{E}^{(2)} = \frac{1}{2}(\boldsymbol{C} - \boldsymbol{I})$ and its conjugate stress tensor, the second Piola–Kirchhoff stress $\boldsymbol{T}^{(2)}$. This is a particularly convenient choice because the second Piola–Kirchhoff stress $\boldsymbol{T}^{(2)}$ is directly obtained as the derivative of the free energy with respect to $\boldsymbol{C}$ using the following standard relationship:

$$\boldsymbol{T}^{(2)} = \frac{\partial \phi}{\partial \boldsymbol{E}^{(2)}} = 2 \frac{\partial \phi}{\partial \boldsymbol{C}}. \tag{26}$$

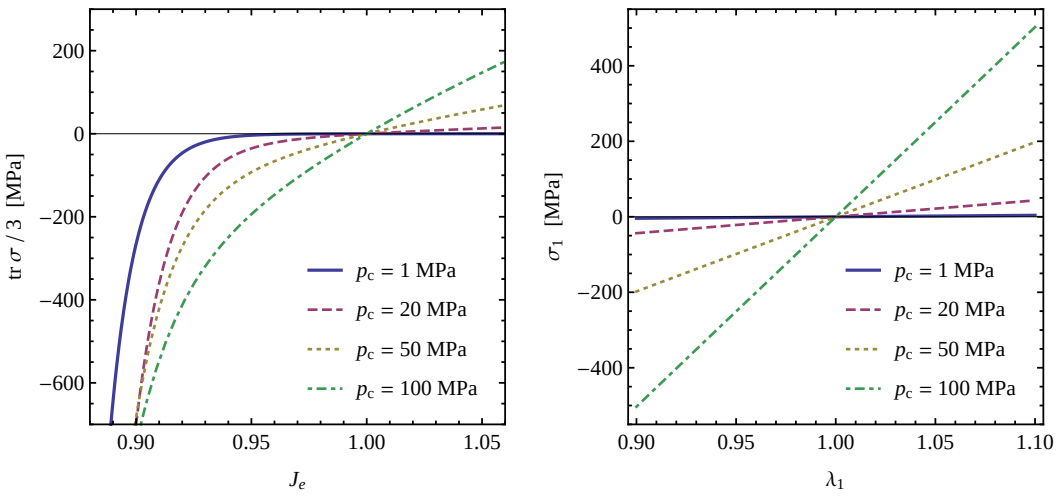

(a) (b)

Figure 1: Nonlinear elasticity accounting for elastoplastic coupling defined by the free energy (21): (a) volumetric deformation, (b) isochoric deformation.

Note that the derivative of the strain energy with respect to $\boldsymbol{E}_e^{(2)} = \frac{1}{2}(\boldsymbol{C}_e - \boldsymbol{I})$ or with respect to $\boldsymbol{C}_e$ yields $\boldsymbol{T}_e^{(2)}$, namely

$$\boldsymbol{T}_e^{(2)} = \frac{\partial \phi}{\partial \boldsymbol{E}_e^{(2)}} = 2\frac{\partial \phi}{\partial \boldsymbol{C}_e}. \tag{27}$$

Clearly, the material response is invariant with respect to the choice of a pair of conjugate strain and stress measures, see [18, 16].

Evaluation of the rate of $\boldsymbol{T}^{(2)}$ defines the inelastic strain rate $\dot{\boldsymbol{E}}_{in}$ according to

$$\dot{\boldsymbol{T}}^{(2)} = \frac{\partial \boldsymbol{T}^{(2)}}{\partial \boldsymbol{E}^{(2)}}[\dot{\boldsymbol{E}}^{(2)}] + \frac{\partial \boldsymbol{T}^{(2)}}{\partial \boldsymbol{C}_p}[\dot{\boldsymbol{C}}_p] + \frac{\partial \boldsymbol{T}^{(2)}}{\partial p_c}\dot{p}_c = \mathbb{E}[\dot{\boldsymbol{E}}^{(2)}] + \mathbb{P}[\dot{\boldsymbol{C}}_p] + \boldsymbol{P}\dot{p}_c = \mathbb{E}[\dot{\boldsymbol{E}}^{(2)} - \dot{\boldsymbol{E}}_{in}], \tag{28}$$

where $\mathbb{E} = \partial \boldsymbol{T}^{(2)}/\partial \boldsymbol{E}^{(2)} = 2\partial \boldsymbol{T}^{(2)}/\partial \boldsymbol{C}$, $\mathbb{P} = \partial \boldsymbol{T}^{(2)}/\partial \boldsymbol{C}_p$, $\boldsymbol{P} = \partial \boldsymbol{T}^{(2)}/\partial p_c$, and

$$\dot{\boldsymbol{E}}_{in} = -\mathbb{E}^{-1}\mathbb{P}[\dot{\boldsymbol{C}}_p] - \mathbb{E}^{-1}[\boldsymbol{P}\dot{p}_c]. \tag{29}$$

3.3 Yield condition

The yield condition is assumed to be defined by the BP yield function (10) expressed in terms of the second Piola-Kirchhoff stress $\boldsymbol{T}_e^{(2)}$ referred to the intermediate configuration,

$$\boldsymbol{T}_e^{(2)} = J_e \boldsymbol{F}_e^{-1}\boldsymbol{\sigma}\boldsymbol{F}_e^{-T} = J_p^{-1}\boldsymbol{F}_p\boldsymbol{T}^{(2)}\boldsymbol{F}_p^T, \tag{30}$$

where $\boldsymbol{\sigma} = J^{-1}\boldsymbol{F}\boldsymbol{T}^{(2)}\boldsymbol{F}^T$ is the Cauchy stress, so that we have

$$F(\boldsymbol{T}_e^{(2)}, p_c) \le 0, \tag{31}$$

and the yield function F is now defined by Eq. (10) through the invariants of $\boldsymbol{T}_e^{(2)}$,

$$p = -\frac{1}{3}\operatorname{tr}\boldsymbol{T}_e^{(2)}, \qquad J_2 = \frac{1}{2}\operatorname{tr}(\operatorname{dev}\boldsymbol{T}_e^{(2)})^2, \qquad J_3 = \frac{1}{3}\operatorname{tr}(\operatorname{dev}\boldsymbol{T}_e^{(2)})^3. \tag{32}$$

The above invariants, and thus the yield function, can be explicitly expressed in terms of the second Piola-Kirchhoff stress $\boldsymbol{T}^{(2)}$ and the plastic right Cauchy–Green tensor $\boldsymbol{C}_p$, the latter playing the role of a hardening variable. Indeed, we have

$$p = -\frac{1}{3} J_p^{-1} \operatorname{tr}(\boldsymbol{T}^{(2)} \boldsymbol{C}_p), \quad J_2 = \frac{1}{2} J_p^{-2} \operatorname{tr}[\operatorname{dev}(\boldsymbol{T}^{(2)} \boldsymbol{C}_p)]^2, \quad J_3 = \frac{1}{3} J_p^{-3} \operatorname{tr}[\operatorname{dev}(\boldsymbol{T}^{(2)} \boldsymbol{C}_p)]^3, \tag{33}$$

which is easily verified in view of the following identity holding for $n = 1, 2, \ldots$,

$$\operatorname{tr}(\boldsymbol{T}_e^{(2)})^n = J_p^{-n} \operatorname{tr}(\boldsymbol{T}^{(2)} \boldsymbol{C}_p)^n, \tag{34}$$

and a similar identity holding for the respective deviators. Note that the yield function was expressed in [11] in terms of the Biot stress tensor referred to the initial configuration.

The parameters p_c and c are defined in the intermediate configuration, while their experimental calibration is performed with respect to the Cauchy stress in the current configuration. In fact, model calibration procedures typically involve the use of the Cauchy or the nominal stress referred to the intermediate configuration, see, for instance, [4]. Although it may seem natural from this perspective to employ those measures of stress, we propose here the choice of the second Piola-Kirchhoff stress, $\boldsymbol{T}_e^{(2)}$. Considering that the elastic strains are relatively small, the stress tensor $\boldsymbol{T}_e^{(2)}$ is, in a sense 'close' to the Cauchy stress tensor $\boldsymbol{\sigma}$, hence provides a physically sound description of the yield surface. At the same time, as shown above, the yield function depending on $\boldsymbol{T}_e^{(2)}$ can be equivalently expressed solely in terms of $\boldsymbol{T}^{(2)}$ and $\boldsymbol{C}_p$ which is not possible if the Cauchy stress is used instead (and would lead to an unsymmetrizing term).[1]

3.4 Plastic flow rule

An *associated flow rule* can be introduced in a straightforward manner as

$$\dot{\boldsymbol{E}}_{in} = \dot{\lambda} \boldsymbol{N}, \qquad \boldsymbol{N} = \frac{\partial F}{\partial \boldsymbol{T}^{(2)}}. \tag{35}$$

However, introducing a non-associative volumetric term, as in the small-strain flow rule (15), requires some consideration.

We start by noting that the rate of deformation tensor $\boldsymbol{d}$, i.e., the symmetric part of the velocity gradient $\boldsymbol{l} = \dot{\boldsymbol{F}} \boldsymbol{F}^{-1}$, is related to the rate of the Green strain tensor $\boldsymbol{E}^{(2)}$ by

$$\boldsymbol{d} = \boldsymbol{F}^{-T} \dot{\boldsymbol{E}}^{(2)} \boldsymbol{F}^{-1}. \tag{36}$$

[1] If the yield function is directly defined in terms of the sole Cauchy stress $\boldsymbol{\sigma}$, the transformation to a function of the second Piola-Kirchhoff stress $\boldsymbol{T}^{(2)}$ imposes a dependence on the total strain, for instance, on $\boldsymbol{C}$, so that

$$F(\boldsymbol{\sigma}) = \tilde{F}(\boldsymbol{T}^{(2)}, \boldsymbol{C}_p, \boldsymbol{C}).$$

If now Prager's consistency, $\dot{F} = 0$, is imposed, the term

$$\frac{\partial \tilde{F}}{\partial \boldsymbol{C}} \cdot \dot{\boldsymbol{C}}$$

yields an unsymmetrizing contribution to the tangent constitutive operator. Therefore, the choice of the Cauchy stress in the yield function leads to a model which does not fit the elastoplasticity framework of [18, 16].

This relationship can be interpreted as a push-forward of $\dot{\boldsymbol{E}}^{(2)}$ to the current configuration. Consider now the following tensor

$$\boldsymbol{d}^* = \boldsymbol{F}_p^{-T}\,\dot{\boldsymbol{E}}^{(2)}\,\boldsymbol{F}_p^{-1} = \boldsymbol{F}_e^{T}\,\boldsymbol{d}\boldsymbol{F}_e, \tag{37}$$

which is a push-forward of $\dot{\boldsymbol{E}}^{(2)}$ to the intermediate configuration. The trace of $\boldsymbol{d}^*$ is equal to

$$\operatorname{tr}\boldsymbol{d}^* = (\boldsymbol{F}_e^{T}\,\boldsymbol{d}\boldsymbol{F}_e)\cdot\boldsymbol{I} = \boldsymbol{d}\cdot\boldsymbol{b}_e = \operatorname{tr}(\boldsymbol{d}\boldsymbol{b}_e). \tag{38}$$

When the elastic strains are small, $\boldsymbol{b}_e$ is close to $\boldsymbol{I}$, and thus the trace of $\boldsymbol{d}^*$ can be used as an approximation of the trace of $\boldsymbol{d}$ which is a measure of the volumetric deformation rate,

$$\operatorname{tr}\boldsymbol{d} \approx \operatorname{tr}\boldsymbol{d}^* \qquad \text{for } \boldsymbol{b}_e \approx \boldsymbol{I}. \tag{39}$$

Using the definition of the inelastic strain rate $\dot{\boldsymbol{E}}_{in}$ in Eq. (28), the push-forward of $\dot{\boldsymbol{E}}^{(2)}$ yields

$$\boldsymbol{d}^* = \boldsymbol{F}_p^{-T}\mathbb{E}^{-1}[\dot{\boldsymbol{T}}^{(2)}]\boldsymbol{F}_p^{-1} + \boldsymbol{F}_p^{-T}\,\dot{\boldsymbol{E}}_{in}\boldsymbol{F}_p^{-1}, \tag{40}$$

where the first term is recognized as the elastic part of $\boldsymbol{d}^*$ and the second term as the inelastic part of $\boldsymbol{d}^*$, thus

$$\boldsymbol{d}^*_{in} = \boldsymbol{F}_p^{-T}\,\dot{\boldsymbol{E}}_{in}\boldsymbol{F}_p^{-1}. \tag{41}$$

In the case of the associated flow rule (35), we have

$$\boldsymbol{d}^*_{in} = \dot{\lambda}\boldsymbol{F}_p^{-T}\boldsymbol{N}\boldsymbol{F}_p^{-1} = \dot{\lambda}J_p^{-1}\boldsymbol{N}_e, \tag{42}$$

where $\boldsymbol{N}_e$ is the gradient of the yield function F evaluated in with respect to $\boldsymbol{T}_e^{(2)}$ with the following transformation rule

$$\boldsymbol{N}_e = \frac{\partial F}{\partial\,\boldsymbol{T}_e^{(2)}} = J_p\boldsymbol{F}_p^{-T}\frac{\partial F}{\partial\,\boldsymbol{T}}\boldsymbol{F}_p^{-1} = J_p\boldsymbol{F}_p^{-T}\boldsymbol{N}\boldsymbol{F}_p^{-1}. \tag{43}$$

The volumetric inelastic strain rate, in the sense of (39), is thus given by

$$\operatorname{tr}\boldsymbol{d}^* = \dot{\lambda}J_p^{-1}\operatorname{tr}\boldsymbol{N}_e. \tag{44}$$

In analogy to the small-strain model, cf. Eq. (15), a *non-associated flow rule* can now be formulated as

$$\boldsymbol{d}^*_{in} = \dot{\lambda}J_p^{-1}\hat{\boldsymbol{N}}_e, \qquad \hat{\boldsymbol{N}}_e = \boldsymbol{N}_e - \frac{1}{3}\,\epsilon(1-\Phi)(\operatorname{tr}\boldsymbol{N}_e)\boldsymbol{I}. \tag{45}$$

By transforming Eq. (45) back to the reference configuration, the flow rule is finally obtained as

$$\dot{\boldsymbol{E}}_{in} = \dot{\lambda}\hat{\boldsymbol{N}}, \qquad \hat{\boldsymbol{N}} = \boldsymbol{N} - \frac{1}{3}\,\epsilon(1-\Phi)\operatorname{tr}(\boldsymbol{N}\boldsymbol{C}_p^{-1})\,\boldsymbol{C}_p, \qquad \boldsymbol{N} = \frac{\partial F}{\partial\,\boldsymbol{T}^{(2)}}. \tag{46}$$

Of course, the flow rule is accompanied by the usual complementarity conditions (16). Note that, as in the small-strain model, the associated flow rule and thus the symmetry of the tangent operator are recovered for $\epsilon = 0$.

4 Finite element implementation

The essential steps involved in derivation and implementation of incremental constitutive relationships are presented in this section. The algorithmic treatment employs the commonly used backward-Euler integration scheme and the classical return mapping algorithm, see, e.g., [1, 2]. The present computer implementation has been carried out using a symbolic code generation system *AceGen* [14], and the related automation is also briefly discussed below.

4.1 Implicit BP yield surface

The BP yield surface $F = 0$ specified by Eqs. (10)–(12) is highly flexible considering the shape of its meridian and deviatoric sections. However, this comes at the cost that the original yield function F is not continuous and, to enforce convexity, is defined infinity for $p \notin [-c, p_c]$. As a result, the BP yield function cannot be effectively evaluated for an arbitrary stress state so that the classical return mapping algorithms cannot be directly applied. A general strategy to overcome this problem, see Stupkiewicz et al. [17], is to introduce an implicitly defined yield function F^* that has the same zero level set $F^* = 0$ as the original yield function, $F = 0$, i.e., the same yield surface, but behaves well for arbitrary stress states. The implicit yield function formulation is followed in this work and is briefly described below. Alternative, less general approaches have been proposed in [19, 20].

Construction of a convex yield function $F^*(\boldsymbol{\sigma}, \cdot)$ generated by a convex yield surface $F(\boldsymbol{\sigma}, \cdot) = 0$ is illustrated in Fig. 2. Consider the (p, q)-space corresponding to a fixed Lode angle θ, and introduce a reference point $(p_r, 0)$ inside the yield surface $F = 0$. In case of the PBG model, a convenient choice for the reference point is $p_r = (p_c + c)/2$. Further, denote by ϱ the distance between the reference point $(p_r, 0)$ and the current stress point (p, q) and by ϱ_0 the distance between the reference point $(p_r, 0)$ and the image point (p_0, q_0) that lies on the yield surface $F = 0$,

$$\varrho = \|\boldsymbol{\varrho}\|, \qquad \varrho_0 = \|\boldsymbol{\varrho}_0\|, \qquad \boldsymbol{\varrho} = (p - p_r, q), \qquad \boldsymbol{\varrho}_0 = (p_0 - p_r, q_0), \tag{47}$$

and we have $\boldsymbol{\varrho}_0/\varrho_0 = \boldsymbol{\varrho}/\varrho$. The yield function F^* is then defined by

$$F^*(\boldsymbol{\sigma}, \cdot) = \frac{\varrho}{\varrho_0} - 1. \tag{48}$$

By construction, the yield function F^* is convex and generates a family of self-similar iso-surfaces $F^* = \text{const}$.

In order to evaluate the yield function $F^*(\boldsymbol{\sigma}, \cdot)$ for an arbitrary stress $\boldsymbol{\sigma}$, a nonlinear equation must be solved to determine ϱ_0. That equation corresponds to the condition that the image point (p_0, q_0) lies on the yield surface. The yield function F^* is thus an *implicit* function. Consequently, its derivatives, for instance, the gradient used in the flow rule, involve the derivatives of the implicit dependence of ϱ_0 on the stress $\boldsymbol{\sigma}$ and, possibly, also on hardening variables. The details can be found in [17].

The present implementation of the PBG model employs the above implicit formulation of the BP yield function. Accordingly, the actual use of the implicit yield function F^* and its gradient $\boldsymbol{N}^*$ is denoted below by a '$*$' in the superscript.

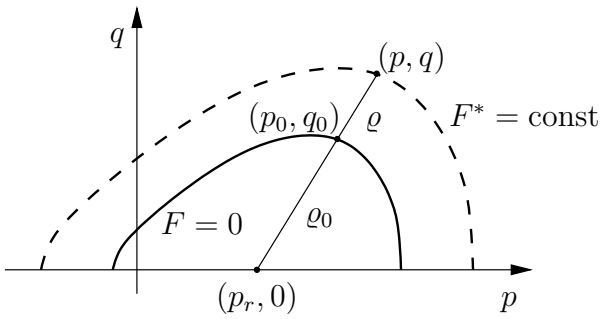

Figure 2: Implicit yield function F^* generated by a convex yield surface $F = 0$.

4.2 Incremental flow rule

With regard to finite element implementation, the constitutive equations specified in Section 3 must be cast in an incremental form, i.e., an appropriate time integration scheme must be applied to the evolution equations for internal variables.

Using the flow rule (46), the rate constitutive equation (28) is rewritten as

$$\dot{\boldsymbol{T}}^{(2)} = \mathbb{E}[\dot{\boldsymbol{E}}^{(2)} - \dot{\lambda}\hat{\boldsymbol{N}}^*], \tag{49}$$

which upon application of the implicit backward-Euler integration scheme yields

$$\boldsymbol{T}^{(2)}_{n+1} - \boldsymbol{T}^{(2)}_{n} = \mathbb{E}_{n+1}[\boldsymbol{E}^{(2)}_{n+1} - \boldsymbol{E}^{(2)}_{n} - \Delta\lambda\hat{\boldsymbol{N}}^*_{n+1}], \tag{50}$$

where $n+1$ and n in the subscript denote, respectively, the current time $t = t_{n+1}$ and the previous time $t = t_n$, at which the corresponding quantities are evaluated. The incremental flow rule (50) is accompanied by the complementarity conditions,

$$F^*_{n+1} = F^*(\boldsymbol{T}^{(2)}_{e,n+1}, p_{c,n+1}) \le 0, \qquad \Delta\lambda \ge 0, \qquad \Delta\lambda F^*_{n+1} = 0, \tag{51}$$

that are enforced at the end of the time increment, consistently with the backward-Euler scheme applied to integrate the rate equation (49).

Considering that arbitrary stress states can be encountered during iterative solution of the return mapping algorithm, the plastic flow direction $\hat{\boldsymbol{N}}^*$ is modified according to

$$\hat{\boldsymbol{N}}^* = \boldsymbol{N}^* - \frac{1}{3}\,\epsilon(1-\Phi_0)\,\mathrm{tr}(\boldsymbol{N}^*\boldsymbol{C}_p^{-1})\,\boldsymbol{C}_p, \qquad \Phi_0 = \frac{p_0 + c}{p_c + c}, \qquad p_0 = \frac{p + F^* p_r}{1 + F^*}. \tag{52}$$

Here, p_0 and Φ_0 are defined such that we have $\Phi_0 \in [0,1]$ for an arbitrary stress just like we have $\Phi \in [0,1]$ for the stresses satisfying $F^* = 0$. As a result, the term specifying the non-associative contribution in Eq. (52) behaves correctly for $F^* \neq 0$. Of course, the flow rule is unaltered for $F^* = 0$, hence the material response is not affected by the above treatment.

Remark 1. The simple backward-Euler scheme is usually avoided in finite-strain plasticity, in particular, in the case of plastically incompressible (or nearly incompressible) materials, e.g., in metal plasticity, and integration schemes employing the exponential map are then preferable, cf. [21, 22]. However, the present plastic flow rule, formulated in terms of the inelastic strain rate $\dot{\boldsymbol{E}}_{in}$ to consistently introduce the elastoplastic coupling, is not well suited for application of an exponential map integrator.

4.3 Constitutive update problem

In the constitutive update problem, given are the deformation gradient $\boldsymbol{F}_{n+1}$ at the current time step and the internal variables $\boldsymbol{C}_{p,n}$ and $p_{c,n}$ at the previous time step, and the goal is to find the current internal variables $\boldsymbol{C}_{p,n+1}$ and $p_{c,n+1}$ and the plastic multiplier $\Delta\lambda$ that satisfy the incremental flow rule (50), the complementarity conditions (51) and the constitutive relationship between $p_{c,n+1}$ and $\boldsymbol{C}_{p,n+1}$ specified by Eq. (25).

The second Piola–Kirchhoff stress $\boldsymbol{T}^{(2)}_{n+1}$, which is needed to evaluate the yield function F^*_{n+1} and its gradient $\boldsymbol{N}^*_{n+1}$ in Eqs. (50)–(52), is defined by the free energy according to

$$\boldsymbol{T}^{(2)}_{n+1} = 2\frac{\partial\phi(\,\boldsymbol{C}_{n+1},\,\boldsymbol{C}_{p,n+1},p_{c,n+1})}{\partial\,\boldsymbol{C}_{n+1}}. \tag{53}$$

The constitutive update problem is solved here using the classical return-mapping algorithm [1, 2]. The trial stress is first computed by assuming that the response is elastic,

$$\boldsymbol{T}^{(2)trial}_{n+1} = 2\frac{\partial\phi(\,\boldsymbol{C}_{n+1},\,\boldsymbol{C}_{p,n},p_{c,n})}{\partial\,\boldsymbol{C}_{n+1}}, \tag{54}$$

for which the trial value of the yield function is evaluated according to

$$F^{*trial}_{n+1} = F^*(\,\boldsymbol{T}^{(2)trial}_{e,n+1},p_{c,n}), \tag{55}$$

where the necessary invariants of $\boldsymbol{T}^{(2)trial}_{e,n+1}$ are expressed in terms of $\boldsymbol{T}^{(2)trial}_{n+1}$ and $\boldsymbol{C}_{p,n}$ using the formulae in Eq. (33).

If $F^{*trial}_{n+1} \le 0$ then the step is elastic, and

$$\boldsymbol{C}_{p,n+1} = \boldsymbol{C}_{p,n}, \qquad p_{c,n+1} = p_{c,n}, \qquad \Delta\lambda = 0. \tag{56}$$

If $F^{*trial}_{n+1} > 0$ then the step is plastic and a set of nonlinear equations must be solved,

$$\mathbf{Q}_{n+1}(\mathbf{h}_{n+1}) = \mathbf{0}, \tag{57}$$

where the vector of unknowns $\mathbf{h}_{n+1}$ comprises the internal variables and the plastic multiplier λ,

$$\mathbf{h}_{n+1} = \{C_{p,11}, C_{p,22}, C_{p,33}, C_{p,12}, C_{p,13}, C_{p,23}, \lambda, p_c\}_{n+1}, \tag{58}$$

and $C_{p,ij}$ denote the components of $\boldsymbol{C}_p$. The local residual vector $\mathbf{Q}_{n+1}$ is defined as

$$\mathbf{Q}_{n+1} = \{\mathcal{Z}_{11}, \mathcal{Z}_{22}, \mathcal{Z}_{33}, \mathcal{Z}_{12}, \mathcal{Z}_{13}, \mathcal{Z}_{23}, F^*_{n+1}, \mathcal{A}_{n+1}\}, \tag{59}$$

where $\mathcal{Z}_{ij}$ are the component-wise residuals corresponding to the incremental flow rule (50),

$$\mathcal{Z}_{ij} = \left(\boldsymbol{T}^{(2)}_{n+1} - \boldsymbol{T}^{(2)}_{n} - \mathbb{E}_{n+1}[\boldsymbol{E}^{(2)}_{n+1} - \boldsymbol{E}^{(2)}_{n} - \Delta\lambda\hat{\boldsymbol{N}}^*_{n+1}]\right)_{ij}, \tag{60}$$

and $\mathcal{A}_{n+1} = 0$ is the equation that relates the hardening variable $p_{c,n+1}$ and the plastic strain $\boldsymbol{C}_{p,n+1}$, cf. Eq. (25),

$$\mathcal{A}_{n+1} = (\det\,\boldsymbol{C}_{p,n+1})^{1/2} - 1 - \mathcal{H}(p_{c,n+1}). \tag{61}$$

Equation (57) is solved using the Newton method according to the following iterative scheme:

$$\mathbf{h}_{n+1}^{(j+1)} = \mathbf{h}_{n+1}^{(j)} + \Delta\mathbf{h}_{n+1}^{(j)}, \qquad \Delta\mathbf{h}_{n+1}^{(j)} = -\left(\frac{\partial \mathbf{Q}_{n+1}}{\partial \mathbf{h}_{n+1}}\right)^{-1} \mathbf{Q}_{n+1}(\mathbf{h}_{n+1}^{(j)}). \tag{62}$$

We note that the internal variables $\mathbf{h}_{n+1}$, being the solution of the constitutive update problem (57), depend on the deformation gradient $\boldsymbol{F}_{n+1}$. This dependence is implicit, and its derivative is obtained by rewriting Eq. (57),

$$\mathbf{Q}_{n+1}(\mathbf{h}_{n+1}(\boldsymbol{F}_{n+1}), \boldsymbol{F}_{n+1}) = \mathbf{0}, \tag{63}$$

and by taking its total derivative with respect to $\boldsymbol{F}_{n+1}$,

$$\frac{\partial \mathbf{Q}_{n+1}}{\partial \mathbf{h}_{n+1}} \frac{\partial \mathbf{h}_{n+1}}{\partial \boldsymbol{F}_{n+1}} + \frac{\partial \mathbf{Q}_{n+1}}{\partial \boldsymbol{F}_{n+1}} = \mathbf{0}, \tag{64}$$

so that the derivative of $\mathbf{h}_{n+1}$ with respect to $\boldsymbol{F}_{n+1}$ is given by

$$\frac{\partial \mathbf{h}_{n+1}}{\partial \boldsymbol{F}_{n+1}} = -\left(\frac{\partial \mathbf{Q}_{n+1}}{\partial \mathbf{h}_{n+1}}\right)^{-1} \frac{\partial \mathbf{Q}_{n+1}}{\partial \boldsymbol{F}_{n+1}}. \tag{65}$$

Remark 2. The present framework of finite-strain elastoplasticity guarantees that the elastoplastic tangent corresponding to constitutive rate equations is symmetric for an associated flow rule, i.e., for $\epsilon = 0$ in Eq. (46), see [11]. It has been checked numerically that the symmetry is not preserved in the incremental setting that is based on the incremental flow rule (50) and the constitutive update problem specified above. However, the symmetry is recovered for the strain increment decreasing to zero. This shows consistency of the present incremental scheme with the rate formulation. Construction of an incremental scheme that would preserve the symmetry of the tangent also for a finite strain increment and would consistently treat the elastoplastic coupling remains an open problem.

Remark 3. In the present implementation, the standard return mapping algorithm specified above has been actually replaced by a more robust algorithm employing the augmented primal closest-point projection method proposed by Perez-Foguet and Armero [23]. This improved algorithm is described in Appendix C.

4.4 Finite element implementation and its automation

The model has been implemented using *AceGen* [13, 14], a symbolic code generation system that combines the symbolic capabilities of *Mathematica* (www.wolfram.com) with the automatic differentiation technique and additional tools for optimization and automatic generation of computer codes. The present formulation of incremental elastoplasticity and the structure of the constitutive update problem fit the general formulation introduced by Korelc [14], hence the automation approach developed in [14] can be directly applied to derive the necessary finite element routines. In particular, the incremental constitutive model is fully defined by specifying the local residual $\mathbf{Q}_{n+1}$ in terms of the internal variables $\mathbf{h}_{n+1}$, as done above, while the remaining part of the formulation remains unaltered. Here and below, all the quantities refer to the current time step $t = t_{n+1}$, and the corresponding subscript will be omitted to simplify the notation.

The main steps of the finite element implementation and its automation are briefly outlined below. The details are omitted here, and an interested reader is referred to [14], see also Section 2 in [24] for a concise presentation of the present automation approach in finite-strain elastoplasticity.

The free energy function, defined by Eq. (21) as function of $\boldsymbol{C}$, $\boldsymbol{C}_p$ and p_c, can be equivalently expressed as a function of the deformation gradient $\boldsymbol{F}$ and the vector of internal variables $\mathbf{h}$, thus $\phi = \phi(\boldsymbol{F}, \mathbf{h})$. The latter form of the free energy corresponds to the actual formulation of the constitutive update problem, as discussed above. The partial derivative of ϕ with respect to $\boldsymbol{F}$ yields the first Piola–Kirchhoff stress tensor $\boldsymbol{P}$,

$$\boldsymbol{P} = \boldsymbol{P}(\boldsymbol{F}, \mathbf{h}) = \frac{\partial \phi(\boldsymbol{F}, \mathbf{h})}{\partial \boldsymbol{F}}. \tag{66}$$

Note that the algorithmic dependence of $\mathbf{h}$ on $\boldsymbol{F}$, as specified by Eq. (65), is suppressed here.

The basis of the finite element formulation is the virtual work principle. For simplicity, we consider here only the internal work contribution and the contribution of the work of surface tractions $\boldsymbol{t}$ on the boundary $\partial\Omega$,

$$\int_\Omega \boldsymbol{P} \cdot \delta \boldsymbol{F} \,\mathrm{d}V - \int_{\partial\Omega} \boldsymbol{t} \cdot \delta \boldsymbol{u} \,\mathrm{d}S = 0. \tag{67}$$

Upon introducing finite element discretization and numerical quadrature, the internal work contribution yields

$$\int_\Omega \boldsymbol{P} \cdot \delta \boldsymbol{F} \,\mathrm{d}V \approx \sum_{e=1}^{n_e} \int_{\Omega_e} \boldsymbol{P} \cdot \delta \boldsymbol{F} \,\mathrm{d}V \approx \sum_{e=1}^{n_e} \delta \mathbf{p}_e \left(\sum_{g=1}^{n_g} w_g \mathbf{R}_g \right). \tag{68}$$

Here, Ω_e denotes the element domain, n_e is the number of elements, and $\mathbf{p}_e$ is the vector of nodal displacements involved in the element e. Further, n_g is the number of integration (Gauss) points per element, w_g is the Gauss-point weight, and $\mathbf{R}_g$ is the Gauss-point residual given by

$$\mathbf{R}_g = \mathbf{R}_g(\mathbf{p}_e, \mathbf{h}_g) = J_g \boldsymbol{P}(\boldsymbol{F}(\mathbf{p}_e), \mathbf{h}_g) \cdot \frac{\partial \boldsymbol{F}}{\partial \mathbf{p}_e}, \tag{69}$$

where $\mathbf{h}_g$ is the vector of internal variables at Gauss point g, and J_g is the Jacobian of transformation from the reference coordinate system of the element to the global coordinate system.

The Gauss-point residuals $\mathbf{R}_g$ form the element residual, i.e., the term in parenthesis in Eq. (68), and the element residuals are assembled in the global residual. As a result, the discrete counterpart of the virtual work principle (67) is finally written as a system of nonlinear equations,

$$\mathbf{R}(\mathbf{p}, \mathbf{h}) = \mathbf{0}, \tag{70}$$

to be solved for the global vector of nodal displacements $\mathbf{p}$. Here, $\mathbf{h}$ denotes the global vector of internal variables which is composed of the individual Gauss-point vectors $\mathbf{h}_g$. The global equilibrium equation (70) together with the Gauss-point equations (57),

$$\mathbf{Q}_g(\boldsymbol{F}(\mathbf{p}_e), \mathbf{h}_g) = \mathbf{0}, \tag{71}$$

form a system of (locally) coupled nonlinear equations that is solved by applying the Newton method in a nested iterative-subiterative scheme [25, 14]. The Gauss-point contribution $\mathbf{K}_g$ to the global tangent matrix is obtained as the total derivative of $\mathbf{R}_g$ with respect to $\mathbf{p}_e$,

$$\mathbf{K}_g = \frac{\partial \mathbf{R}_g}{\partial \mathbf{p}_e} + \frac{\partial \mathbf{R}_g}{\partial \mathbf{h}_g}\frac{\partial \mathbf{h}_g}{\partial \boldsymbol{F}}\frac{\partial \boldsymbol{F}}{\partial \mathbf{p}_e} = \frac{\partial \mathbf{R}_g}{\partial \mathbf{p}_e} - \frac{\partial \mathbf{R}_g}{\partial \mathbf{h}_g}\left(\frac{\partial \mathbf{Q}_g}{\partial \mathbf{h}_g}\right)^{-1}\frac{\partial \mathbf{Q}_g}{\partial \boldsymbol{F}}\frac{\partial \boldsymbol{F}}{\partial \mathbf{p}_e} \tag{72}$$

where the algorithmic dependence of $\mathbf{h}_g$ on $\boldsymbol{F}$, see Eq. (65), has been taken into account.

The practical computer implementation using the *AceGen* system is directly based on the above formalism. In particular, once the constitutive functions and the structure of the constitutive update problem are specified, derivation of all the necessary expressions and generation of the corresponding computer code is automatized. Application of the automatic differentiation technique[2] implemented in *AceGen* results in exact linearization of the incremental constitutive relationships so that an exact consistent (algorithmic) tangent matrix is obtained, which normally is not a trivial task for a complex material model. This is highly beneficial for the overall performance of the Newton-based computational scheme applied to solve the global equilibrium equations.

5 Numerical examples

5.1 Experimental validation of the model

Parameters of the small-strain PBG model have been calibrated for alumina powder in [10]. In [15], predictions of the present finite-strain PBG model have been successfully verified against an extended set of experimental data with a minor modification of model parameters with respect to those used in [10] for the small-strain model. Selected results from [15] are reported below in order to illustrate the ability of the model to properly describe the behaviour of the alumina powder subjected to uniform and nonuniform compaction.

Model parameters for alumina powder used in the present study are provided in Table 1. The parameters are taken from [15] with only one modification: the value of parameter μ_0 has been increased with respect to that adopted in [10, 15] since it has been noticed that the latter may lead to exceedingly large elastic shear strains at small values of the forming pressure p_c. At the same time, in compression-dominated processes, such as those considered in [10, 15] and in the present paper, the overall response is not significantly affected. In fact, the results presented in this subsection are very close to those reported in [15] for the original set of model parameters.

Response in uniform uniaxial compression is compared to experiment in Fig. 3. Experimental data are taken from [10] and refer to compaction of cylindrical specimens between flat punches, as illustrated in the insets in Fig. 3. The ratio of the initial height (8.7 mm) to the diameter (30 mm) is small so that the effect of friction at the die wall is negligible, and the deformation can be assumed uniform within the specimen. The simulated force versus punch displacement curves are reported for the maximum compaction pressure of 60 and 120 MPa. The agreement with experiment is excellent both for the finite-strain

[2]It is recalled that automatic differentiation is not numerical differentiation, and, unlike numerical differentiation, it is free of round-off errors.

Table 1: Material parameters for alumina powder.

M	m	α	β	γ	ϵ	$\tilde{a}_1$	$\tilde{a}_2$	Λ_1 (MPa)	Λ_1 (MPa)
1.1	2	0.1	0.19	0.9	0.5	0.383	0.124	1.8	40
c_∞ (MPa)	Γ (MPa^{-1})	p_{cb} (MPa)	B (MPa^{-1})	n	μ_0 (MPa)	μ_1	κ	e_0	p_0 (MPa)
2.3	0.026	3.2	0.18	6	20	64	0.04	2.129	0.063

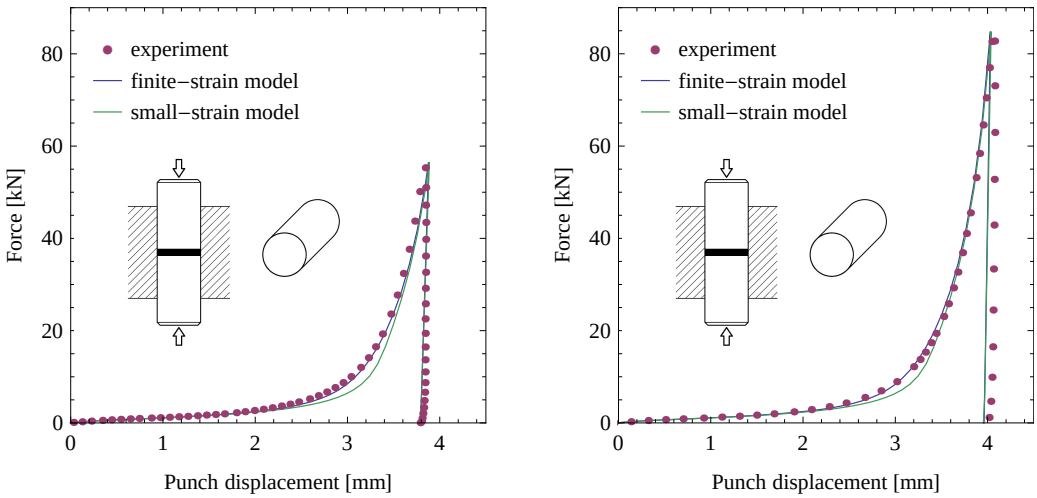

(a) (b)

Figure 3: Predictions of the small- and finite-strain versions of the PBG model for uniform compression of alumina powder by a flat punch: (a) compaction at 60 MPa, (b) compaction at 120 MPa. Experimental data are taken from [10].

model and for the small-strain model. The latter is simulated using the parameters provided in Table 1 with parameter $B = 0.6$ MPa^{-1} adjusted such that the uniaxial response of the two models is as close as possible, see [15].

As the second example, we study forming of alumina powder in a mould with a cross-shaped punch, see Fig. 4. This process is characterized by a highly inhomogeneous deformation. The corresponding experimental data are taken from [15], where a cross-shaped punch of 30 mm diameter and with 2.5 mm deep grooves has been used to form pieces from 8 g of alumina at a vertical load of 70 kN.

The undeformed finite-element mesh of one quarter of the piece is shown in Fig. 5a. Simplified boundary conditions have been applied in the simulation. The displacements are fully constrained at the bottom surface, and the loading is applied by prescribing the vertical displacement at the top surface with constrained horizontal displacements. Those boundary conditions correspond to high friction that results in sticking contact at the bottom and top surfaces. On the lateral surface, the horizontal displacements are constrained and the vertical displacement is free. This approximately corresponds to frictionless contact at the lateral surface. As the initial aspect ratio of the specimen is small, the effect of friction at the lateral surface on the forming force and on the deformation pattern is expected to be small. One quarter of the piece is simulated, and normal displacements are constrained on the symmetry planes. The eight-node hexahedral F-bar element [26] has been used in the present computations.

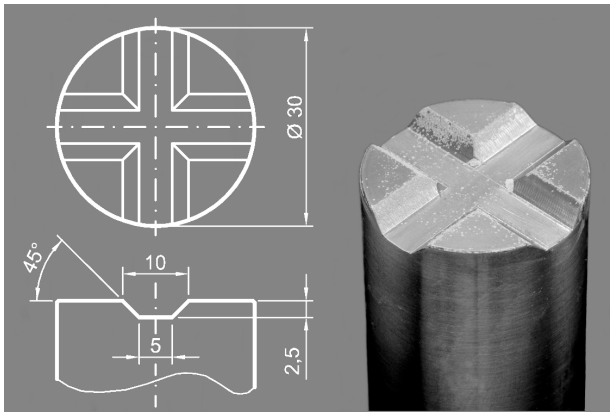

Figure 4: The cross-shaped punch (dimensions in mm) used in the experiment [15].

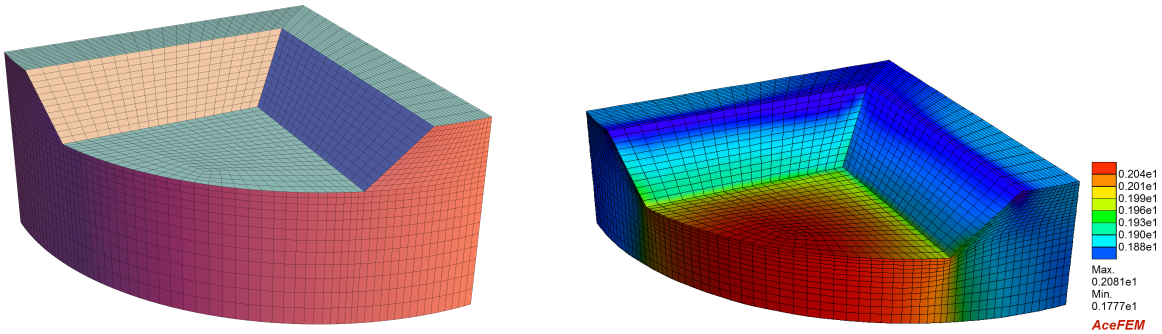

(a) (b)

Figure 5: Cross-shaped piece (one quarter is simulated): (a) finite element mesh (19,968 elements and 66,044 displacement unknowns), (b) distribution of density (in g/cm^3) in the final deformed configuration.

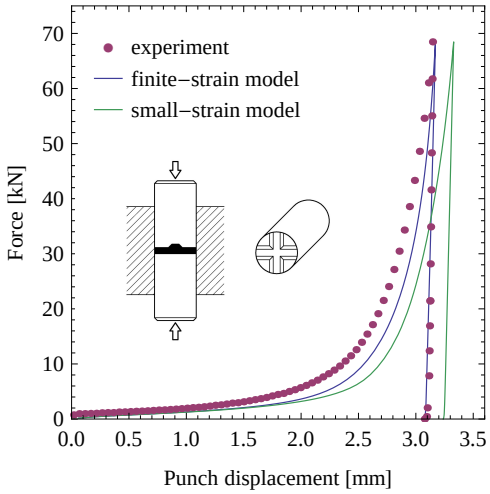

Figure 6: Predictions of the small- and finite-strain versions of the PBG model for compression of alumina powder by the cross-shaped punch (nonuniform 3D deformation). Experimental data are taken from [15].

Unloading of the punch is simulated by gradually decreasing to zero the reaction forces at the bottom and top surfaces. Subsequently, the reaction forces at the lateral surface are gradually decreased to zero to simulate spring-back during ejection from the mould. Both steps are accompanied by plastic deformation that is caused by residual stresses within the specimen.

The simulated and experimental force versus punch displacement curves are compared in Fig. 6. The agreement with experimental data is satisfactory for the finite-strain model and is noticeably worse for the small-strain model. This is not surprising considering that large and nonuniform deformations are involved with the volumetric deformation locally reaching $J_p = 0.5$. The final distribution of density is shown in Fig. 5b in the deformed configuration, which also shows a large reduction of the overall height of the piece with respect to the initial configuration (Fig. 5a).

Nonuniform deformations and the related nonuniform hardening of the piece are also illustrated in Fig. 7a. As shown, the local values of cohesion c vary between 0.25 MPa and 2.29 MPa, where the latter value is close to the maximum cohesion specified by parameter $c_\infty = 2.3$ MPa. Figure 7b shows the reduction of cohesion during unloading and spring-back. The maximum reduction occurs at the groove edges, and the associated plastic softening may lead to damage of the piece. Indeed, some samples did break exactly at this location, see [15].

Robustness of the present implementation of the model is illustrated in Fig. 8. It is shown that the solution can proceed with large time increments so that the whole simulation can be completed in only 22 time steps (using an adaptive time incrementation scheme). Moreover, the response obtained using the large steps is practically identical to that obtained using much smaller time increments (about 100 step in the loading phase), as indicated by the solid line in Fig. 8. The high robustness has been achieved thanks to the enhanced return mapping algorithm described in Appendix C. Also, the Newton method at the global level performs very well thanks to the exact linearization of the incremental constitutive relationships (consistent tangent), which is crucial for achieving the quadratic convergence rate. As described above, the linearization has been seamlessly

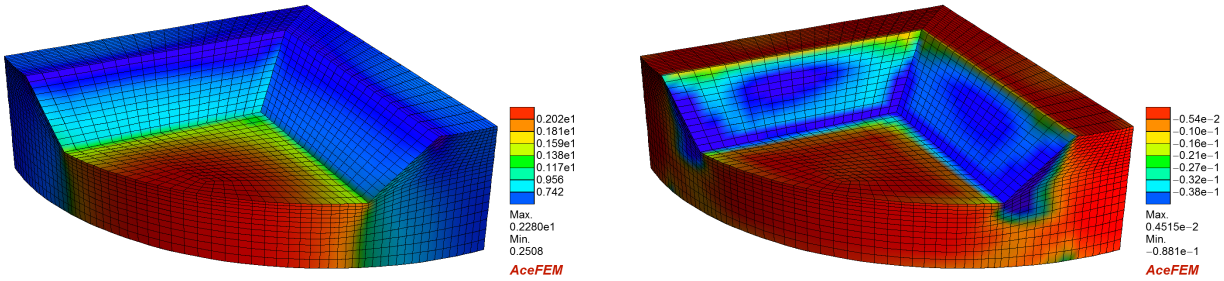

(a) (b)

Figure 7: Cross-shaped specimen: distributions of (a) cohesion c (in MPa) after spring-back and (b) change in cohesion Δc during spring-back.

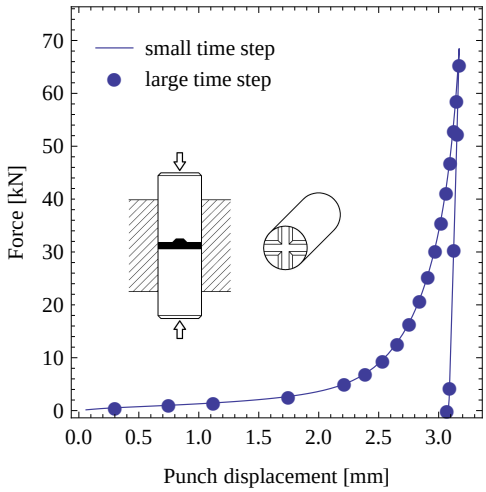

Figure 8: Compaction by a cross-shaped punch: force-displacement response predicted for small time steps and for large time steps.

carried out using the automatic differentiation technique and the *AceGen* system.

5.2 Compaction in a cylindrical die: effect of die-wall friction

In this section, compaction of an alumina powder in a cylindrical die is considered with account for die-wall friction, and the effect of friction coefficient and initial aspect ratio is studied in detail.

Consider thus cold compression of alumina powder into a rigid cylindrical mould of radius r. The powder specimen has an initial height h_0 and is compressed by a rigid punch with a maximum force corresponding to the average compaction pressure of 160 MPa. Three values of the initial aspect ratio of the alumina sample are employed, $h_0/r = 2$, 4 and 6. Coulomb friction is assumed at the powder-mould and powder-punch contact interfaces, and three values of the friction coefficient are used, $\mu = 0.1$, 0.3 and 0.5. Material parameters corresponding to alumina powder are provided in Table 1.

In the finite element implementation, an axisymmetric under-integrated four-node element employing the volumetric-deviatoric split and Taylor expansion of shape functions [27] is used for the solid, and the augmented Lagrangian method used to enforce the frictional contact constraints [28, 29].

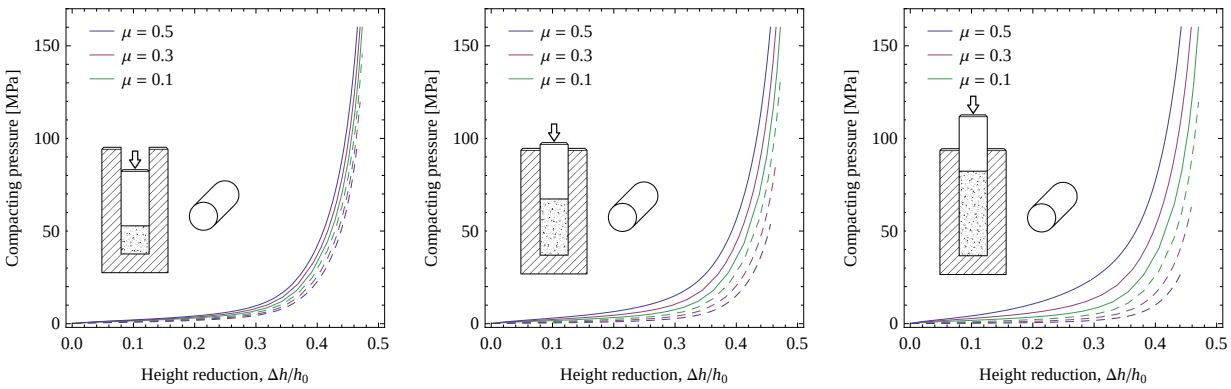

(a) (b) (c)

Figure 9: The average compacting pressure (solid lines) and the average pressure at the bottom part of the mould (dashed lines) as a function of the height reduction $\Delta h/h_0$ for: (a) $h_0/r = 2$, (b) $h_0/r = 4$, (c) $h_0/r = 6$.

The effect of friction coefficient μ and initial aspect ratio h_0/r is illustrated in Fig. 9 which shows the average compacting pressure as a function of the height reduction $\Delta h/h_0$. In each case, in addition to the compacting pressure indicated by a solid line, the corresponding average pressure at the bottom part of the mould is also shown using a dashed line of the same color. Clearly, for frictionless contact at the die wall, the two pressures would be equal one to the other, and the difference increases with increasing friction coefficient μ and with increasing initial aspect ratio h_0/r.

The finite element mesh representing one half of the cross-section of the (axisymmetric) sample is shown in Fig. 10 for $h_0/r = 2$ and $h_0/r = 6$. The undeformed mesh is shown in the left column, and the deformed meshes corresponding to the maximum compression force and different friction coefficients are shown aside. The color map, identical for all figures, indicates the resulting density of alumina powder. Due to friction, the density is nonuniform within the cross-section of the specimen, and the substantial effect of friction coefficient μ and initial aspect ratio h_0/r on the density distribution is clearly seen in Fig. 10.

The effect of friction, which is more pronounced for higher aspect ratios, results in reduced overall compaction so that the final height corresponding to the same prescribed maximum compression force depends on the friction coefficient. This is particularly visible for $h_0/r = 6$. Also, the deformation pattern is affected by the shear stresses due to friction at the die wall, which is seen in the distortion of the initially rectangular mesh.

In the PBG model, plastic hardening is governed by the volumetric plastic deformation. Nonuniform distribution of density results thus in nonuniform hardening within the sample. This is illustrated in Fig. 11 which shows the distribution of the cohesion c, again indicated by the same color map for all figures. The pattern of inhomogeneity of c is qualitatively similar to that shown in Fig. 10, and the same applies to the distribution of the forming pressure p_c (not shown for brevity).

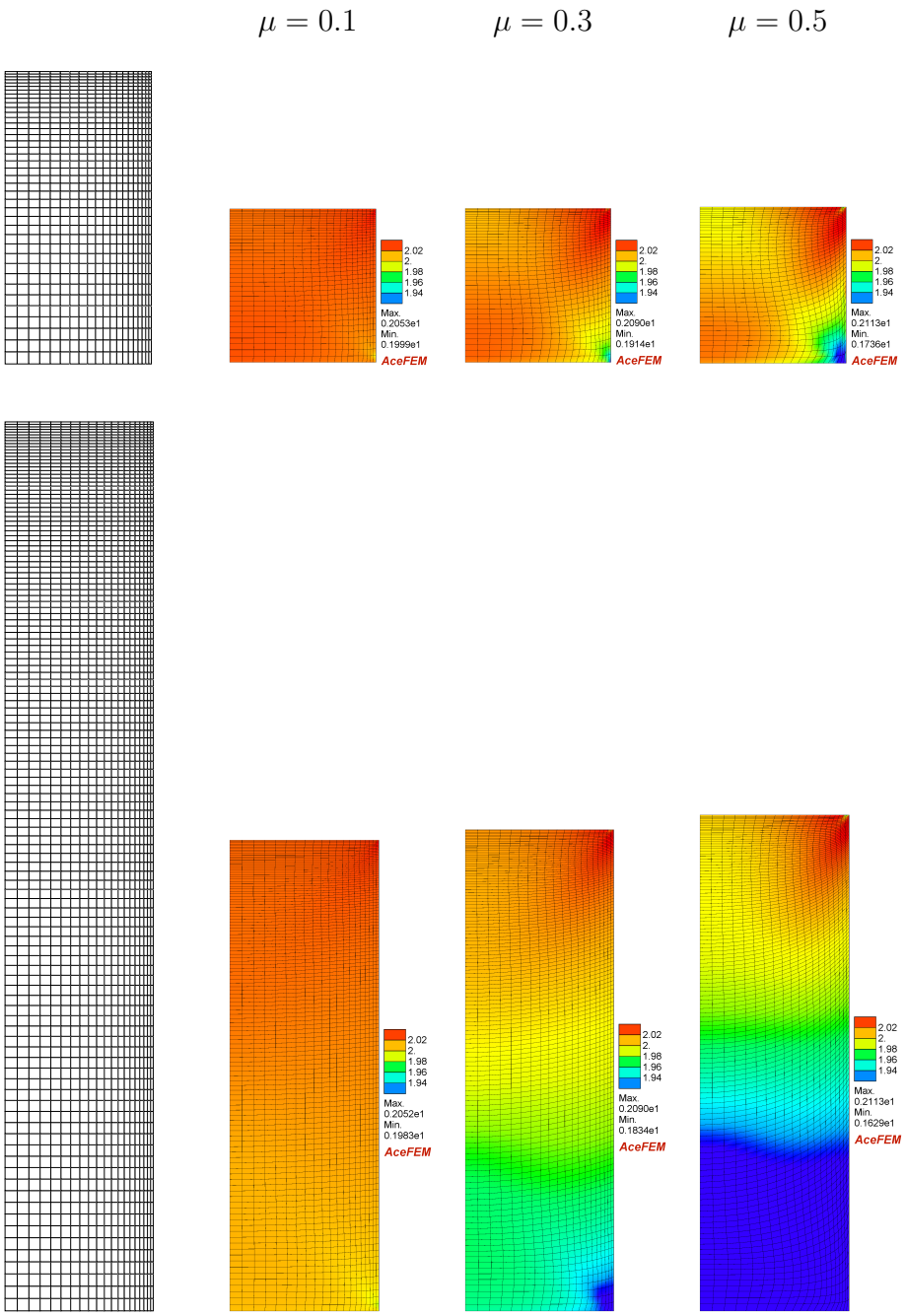

Figure 10: Axisymmetric compression into a rigid cylindrical mould: the undeformed mesh (left) and the deformed mesh corresponding to a prescribed maximum force and different friction coefficients μ for $h_0/r = 2$ (upper row) and $h_0/r = 6$ (lower row). The color map, identical for all figures, indicates the density (in g/cm^3).

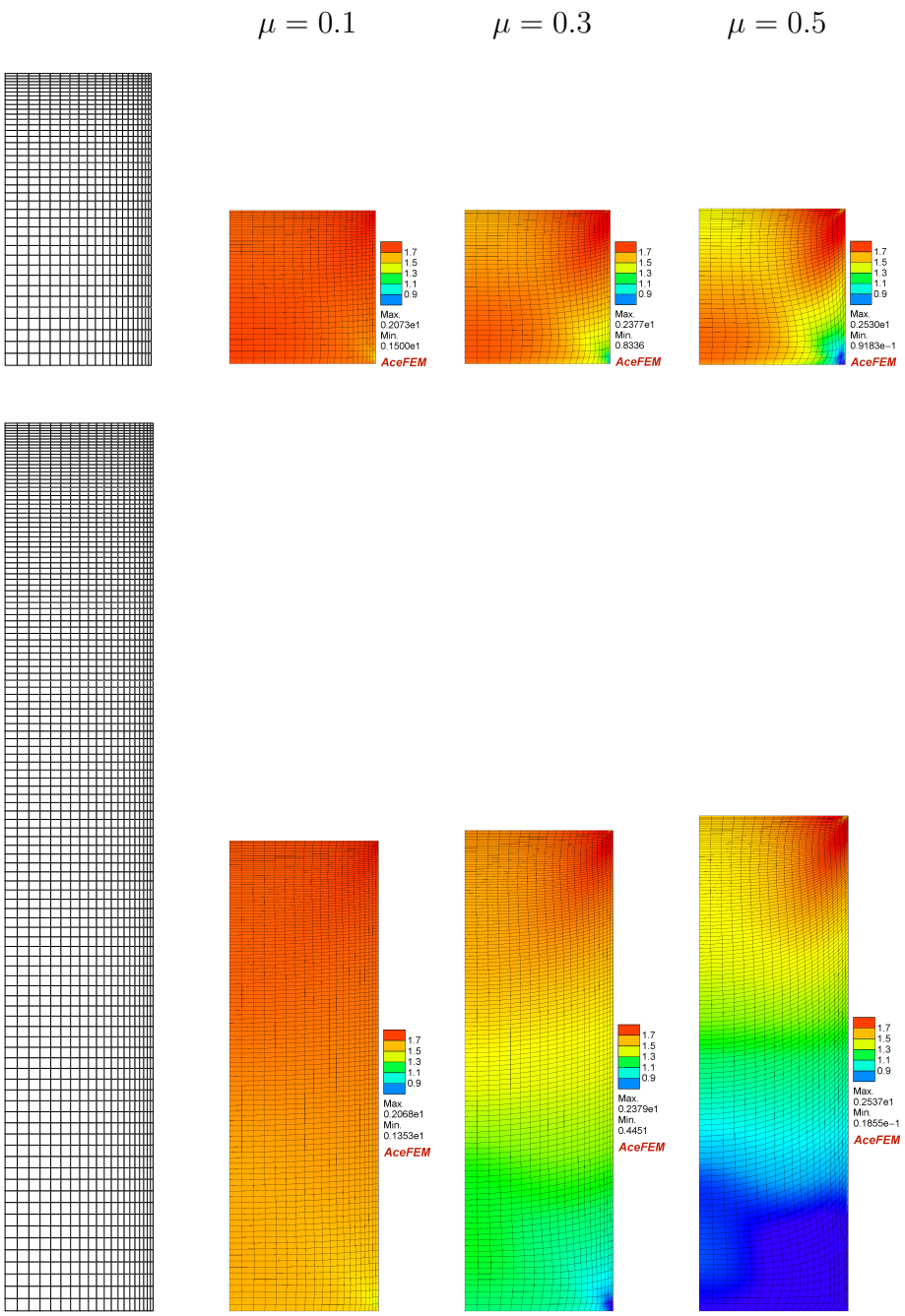

Figure 11: Axisymmetric compression into a rigid cylindrical mould: the undeformed mesh (left) and the deformed mesh corresponding to a prescribed maximum force and different friction coefficients μ for $h_0/r = 2$ (upper row) and $h_0/r = 6$ (lower row). The color map, identical for all figures, indicates the cohesion c (in MPa).

6 Conclusion

A finite strain model for powder compaction has been developed through the derivation of an incremental scheme allowing the successful FE implementation of a series of 'non-standard' constitutive features, including: (i.) nonlinear elastic behaviour even at small strain; (ii.) coupling between elastic and plastic deformation; (iii.) pressure- and J_3-dependent yielding; (iv.) non-isochoric flow. The extension of concepts established at small strain to the large deformation context has required a proper selection of the stress variable to be employed for the yield function and the definition of a neo-Hookean 'correction' to the small strain elastic potential. An incremental scheme compatible with the finite-strain formulation of elastoplastic coupling has also been developed. The numerical tests performed on the model have indicated a correct and robust behaviour of the developed code and have demonstrated the possibility of accurate simulation of the transition from a granular material to a fully dense body occurring during the cold forming of ceramic powders.

Acknowledgments

The authors gratefully acknowledge financial support from European Union FP7 project under contract number PIAP-GA-2011-286110.

A Free energy expressed in terms of the logarithmic elastic strain $\boldsymbol{\epsilon}_e$

In this appendix, we provide the formulation corresponding to the original form of the free energy function as proposed in [11]. Consider thus the small-strain free energy function (2) with the infinitesimal elastic strain $\boldsymbol{\varepsilon}_e$ simply replaced by the logarithmic elastic strain $\boldsymbol{\epsilon}_e$, viz.

$$\phi(\boldsymbol{C}, \boldsymbol{C}_p, p_c) = c\ \mathrm{tr}\,\boldsymbol{\epsilon}_e + (p_0+c)\left[\left(d-\frac{1}{d}\right)\frac{(\mathrm{tr}\,\boldsymbol{\epsilon}_e)^2}{2\tilde{\kappa}} + d^{1/n}\tilde{\kappa}\exp\left(-\frac{\mathrm{tr}\,\boldsymbol{\epsilon}_e}{d^{1/n}\tilde{\kappa}}\right)\right] + \mu\,\mathrm{tr}\,\boldsymbol{\epsilon}_e^2 - \frac{\mu}{3}(\mathrm{tr}\,\boldsymbol{\epsilon}_e)^2. \tag{73}$$

The difference with respect to the free energy function (21) concerns the shear response introduced by the last two terms in Eq. (73). We also note that, in the original form [11], the logarithmic plastic strain $\boldsymbol{E}_p^{(0)}$ has been adopted as the internal variable rather than the plastic right Cauchy–Green tensor $\boldsymbol{C}_p$. The two tensors are related by Eq. $(20)_2$, or by the inverse relationship $\boldsymbol{C}_p = \exp(2\boldsymbol{E}_p^{(0)})$, hence both formulations are equivalent. As shown below, explicit formulae involving $\boldsymbol{C}_p$ are readily available, hence using $\boldsymbol{E}_p^{(0)}$ as the internal variable would introduce an additional and unnecessary complexity related to the tensor exponential function relating $\boldsymbol{E}_p^{(0)}$ and $\boldsymbol{C}_p$.

The free energy (73) is expressed in terms of two invariants of the logarithmic elastic strain $\boldsymbol{\epsilon}_e$, namely $\mathrm{tr}\,\boldsymbol{\epsilon}_e$ and $\mathrm{tr}\,\boldsymbol{\epsilon}_e^2$. Evaluation of the former does not pose any difficulties, see Eqs. (23)–(24). In order to compute the second invariant, $\mathrm{tr}\,\boldsymbol{\epsilon}_e^2$, the logarithmic elastic strain $\boldsymbol{\epsilon}_e$ must be computed explicitly (this has been avoided in the case of the first

invariant $\operatorname{tr}\boldsymbol{\epsilon}_e$). In view of Eqs. $(18)_3$ and $(20)_1$, we have

$$\boldsymbol{\epsilon}_e = \frac{1}{2}\log(\boldsymbol{F}\boldsymbol{C}_p^{-1}\boldsymbol{F}^T). \tag{74}$$

However, this expression involves the deformation gradient $\boldsymbol{F}$ and not the right Cauchy–Green tensor $\boldsymbol{C}$. Note that an explicit dependence on $\boldsymbol{C}$ (or equivalently on $\boldsymbol{E}^{(2)}$) is needed in the present elastoplasticity framework, see Eqs. (26)–(28). Due to objectivity, the free energy function is invariant to a rigid-body rotation, hence we have

$$\operatorname{tr}\boldsymbol{\epsilon}_e^2 = \operatorname{tr}(\boldsymbol{\epsilon}_e^*)^2, \qquad \boldsymbol{\epsilon}_e^* = \frac{1}{2}\log(\boldsymbol{U}\boldsymbol{C}_p^{-1}\boldsymbol{U}) = \frac{1}{2}\log(\boldsymbol{C}^{1/2}\boldsymbol{C}_p^{-1}\boldsymbol{C}^{1/2}), \tag{75}$$

where $\boldsymbol{\epsilon}_e^*$ refers to a special configuration rotated by $\boldsymbol{R} = \boldsymbol{F}\boldsymbol{U}^{-1}$ with respect to the current configuration. It is seen that the resulting formula (75) for $\operatorname{tr}\boldsymbol{\epsilon}_e^2$ is rather complex as it involves the tensor logarithm function and the square root of $\boldsymbol{C}$. Even more importantly, if the above formulation was adopted, then solution of the constitutive update problem would involve the third derivative the tensor logarithm function, which would be associated with a prohibitively high computational cost.

Considering that the elastic strains are relatively small in the materials of interest, the second invariant $\operatorname{tr}\boldsymbol{\epsilon}_e^2$ can be approximated with a high accuracy by exploiting the following approximation of the logarithmic strain, see [30],

$$\boldsymbol{\epsilon}_e = \log\,\boldsymbol{V}_e \approx \frac{1}{2}(\,\boldsymbol{V}_e - \,\boldsymbol{V}_e^{-1}), \tag{76}$$

which leads to

$$\operatorname{tr}\boldsymbol{\epsilon}_e^2 \approx \frac{1}{4}(\operatorname{tr}\boldsymbol{b}_e + \operatorname{tr}\boldsymbol{b}_e^{-1} - 6) = \frac{1}{4}[\operatorname{tr}(\boldsymbol{C}\boldsymbol{C}_p^{-1}) + \operatorname{tr}(\boldsymbol{C}\boldsymbol{C}_p^{-1})^{-1} - 6]. \tag{77}$$

Concluding, the free energy function (73) can be directly expressed in terms of $\boldsymbol{C}$ and $\boldsymbol{C}_p$ using Eq. (24) for $\operatorname{tr}\boldsymbol{\epsilon}_e$ and Eq. (75) or (77) for $\operatorname{tr}\boldsymbol{\epsilon}_e^2$.

B Convexity and strong ellipticity for the free energy (21)

Convexity of the strain energy expressed as a function of the logarithmic strain is a property sufficient to exclude material softening, namely, a descending branch in the Cauchy-stress/logarithmic-strain representation. For a granular material, nonconvexity of the strain energy (21) as a function of the logarithmic strain would be undesired. In fact, we prove in the following that the free energy (21) is a convex function of $\boldsymbol{\epsilon}_e$. The convexity of the representation of the strain energy as a function of the deformation gradient is a different issue, so that a convex function of $\boldsymbol{\epsilon}_e$ can be nonconvex in $\boldsymbol{F}_e$. In this case, it is important to show that, although not convex, this function satisfies the strong ellipticity condition (which implies ellipticity) within a range of elastic deformation compatible with the behaviour of a granular material. In fact ellipticity prevents the possibility of a purely elastic strain localization, that would be unrealistic to occur in a granular medium. In the following strong ellipticity of the elastic branch of the constitutive equation is shown to hold up to an elastic strain of 15%.

Convexity of the free energy as a function of the logarithmic strain. The free energy function (21) is convex in the variable $\boldsymbol{\epsilon}_e$, because it is a sum of convex functions, as shown below. The first three terms (linear, quadratic, exponential) in eq (21) are clearly convex. The fourth term $\bar{I}_2$ requires more attention. It can be written as

$$\bar{I}_2 = \frac{\operatorname{tr} e^{2\boldsymbol{\epsilon}_e}}{e^{2/3\operatorname{tr}\boldsymbol{\epsilon}_e}}. \tag{78}$$

Using Hill's result [31] (convexity of an isotropic function of a symmetric tensor is equivalent to convexity of the corresponding function of the principal values), we are left with the proof of convexity of the function

$$\bar{I}_2 = \frac{e^{2x} + e^{2y} + e^{2z}}{e^{2/3(x+y+z)}}. \tag{79}$$

The corresponding Hessian matrix is

$$\frac{4}{9}e^{-\frac{2}{3}(x+y+z)} \begin{pmatrix} 4e^{2x} + e^{2y} + e^{2z} & e^{2z} - 2\left(e^{2x} + e^{2y}\right) & e^{2y} - 2\left(e^{2x} + e^{2z}\right) \\ e^{2z} - 2\left(e^{2x} + e^{2y}\right) & e^{2x} + 4e^{2y} + e^{2z} & e^{2x} - 2\left(e^{2y} + e^{2z}\right) \\ e^{2y} - 2\left(e^{2x} + e^{2z}\right) & e^{2x} - 2\left(e^{2y} + e^{2z}\right) & e^{2x} + e^{2y} + 4e^{2z} \end{pmatrix}, \tag{80}$$

having principal minors

$$H_1 = \frac{4}{9}e^{-\frac{2}{3}(x+y+z)}\left(4e^{2x} + e^{2y} + e^{2z}\right), \tag{81}$$

$$H_2 = \frac{16}{9}e^{-\frac{4}{3}(x+y+z)}\left(e^{2(x+y)} + e^{2(x+z)} + e^{2(y+z)}\right), \tag{82}$$

$$H_3 = 0, \tag{83}$$

which are clearly non-negative, so that convexity follows.

Strong ellipticity for the free energy. The free energy (21) can be equivalently written in terms of $\boldsymbol{F}_e$ as

$$\phi(\boldsymbol{F}_e) = f_{\text{vol}}(\log J_e) + \frac{\mu}{2}\left[\frac{1}{J_e^{2/3}}\operatorname{tr}(\boldsymbol{F}_e\boldsymbol{F}_e^T) - 3\right], \tag{84}$$

where the *volumetric* function f_{vol} is defined as

$$f_{\text{vol}}(x) = c\,x + (p_0 + c)\left[\left(d - \frac{1}{d}\right)\frac{x^2}{2\tilde{\kappa}} + d^{1/n}\tilde{\kappa}\exp\left(-\frac{x}{d^{1/n}\tilde{\kappa}}\right)\right]. \tag{85}$$

The first Piola-Kirchhoff stress tensor is given by

$$\boldsymbol{S} = \frac{\partial\phi}{\partial\boldsymbol{F}_e} = f'_{\text{vol}}(\log J_e)\boldsymbol{F}_e^{-T} + \frac{\mu}{J_e^{2/3}}\left[\boldsymbol{F}_e - \frac{\operatorname{tr}(\boldsymbol{F}_e\boldsymbol{F}_e^T)}{3}\boldsymbol{F}_e^{-T}\right], \tag{86}$$

and the tangent constitutive operator by

$$\begin{aligned}\mathbb{C} = \frac{\partial^2\phi}{\partial\boldsymbol{F}_e^2} &= f''_{\text{vol}}(\log J_e)\boldsymbol{F}_e^{-T}\otimes\boldsymbol{F}_e^{-T} - f'_{\text{vol}}(\log J_e)\boldsymbol{F}_e^{-T}\,\overline{\otimes}\,\boldsymbol{F}_e^{-1} \\ &+ \frac{\mu}{J_e^{2/3}}\left[\mathbb{I} - \frac{2}{3}\left(\boldsymbol{F}_e\otimes\boldsymbol{F}_e^{-T} + \boldsymbol{F}_e^{-T}\otimes\boldsymbol{F}_e\right) + \frac{2}{9}\operatorname{tr}(\boldsymbol{F}_e\boldsymbol{F}_e^T)\boldsymbol{F}_e^{-T}\otimes\boldsymbol{F}_e^{-T}\right. \\ &\left. + \frac{1}{3}\operatorname{tr}(\boldsymbol{F}_e\boldsymbol{F}_e^T)\boldsymbol{F}_e^{-T}\,\overline{\otimes}\,\boldsymbol{F}_e^{-1}\right],\end{aligned} \tag{87}$$

where $\mathbb{I}$ is the fourth-order identity tensor and two tensorial products between second-order tensors $\boldsymbol{A}$ and $\boldsymbol{B}$ have been employed, which can be defined, with reference to every tensor $\boldsymbol{C}$, as (see also [11])

$$(\boldsymbol{A}\otimes\boldsymbol{B})[\boldsymbol{C}]=(\boldsymbol{B}\cdot\boldsymbol{C})\boldsymbol{A},\qquad(\boldsymbol{A}\,\overline{\otimes}\,\boldsymbol{B})[\boldsymbol{C}]=\boldsymbol{A}\boldsymbol{C}^T\boldsymbol{B}^T. \tag{88}$$

The acoustic tensor $\boldsymbol{A}(\boldsymbol{n})$ is obtained from the formula $\mathbb{C}[\boldsymbol{g}\otimes\boldsymbol{n}]\boldsymbol{n}=\boldsymbol{A}(\boldsymbol{n})\boldsymbol{g}$, where $\boldsymbol{n},\boldsymbol{g}$ are unit vectors, and reads

$$\begin{aligned}\boldsymbol{A}(\boldsymbol{n})=\frac{\mu}{J_e^{2/3}}\left[\boldsymbol{I}-\frac{2}{3}\left(\boldsymbol{F}_e\boldsymbol{n}\otimes\boldsymbol{F}_e^{-T}\boldsymbol{n}+\boldsymbol{F}_e^{-T}\boldsymbol{n}\otimes\boldsymbol{F}_e\boldsymbol{n}\right)\right]\\+\left[f''_{\rm vol}(\log J_e)-f'_{\rm vol}(\log J_e)+\frac{5\mu}{9J_e^{2/3}}\,{\rm tr}(\boldsymbol{F}_e\boldsymbol{F}_e^T)\right]\boldsymbol{F}_e^{-T}\boldsymbol{n}\otimes\boldsymbol{F}_e^{-T}\boldsymbol{n}.\end{aligned} \tag{89}$$

Strong ellipticity is the condition of positive definiteness of the acoustic tensor, namely, $\boldsymbol{g}\cdot\boldsymbol{A}(\boldsymbol{n})\boldsymbol{g}>0$ for every non-zero unit vectors $\boldsymbol{n}$ and $\boldsymbol{g}$. We obtain

$$\begin{aligned}\boldsymbol{g}\cdot\boldsymbol{A}(\boldsymbol{n})\boldsymbol{g}=\frac{\mu}{J_e^{2/3}}\Big[1-\frac{4}{3}(\boldsymbol{F}_e^{-T}\boldsymbol{n}\cdot\boldsymbol{g})(\boldsymbol{F}_e\boldsymbol{n}\cdot\boldsymbol{g})+\frac{5}{9}\,{\rm tr}(\boldsymbol{F}_e\boldsymbol{F}_e^T)(\boldsymbol{F}_e^{-T}\boldsymbol{n}\cdot\boldsymbol{g})^2\Big]\\+\Big[f''_{\rm vol}(\log J_e)-f'_{\rm vol}(\log J_e)\Big](\boldsymbol{F}_e^{-T}\boldsymbol{n}\cdot\boldsymbol{g})^2.\end{aligned} \tag{90}$$

The second term in (90) is always positive (the fact that $[f''_{\rm vol}-f'_{\rm vol}]$ is positive has been checked for a large range of volumetric deformations). It can be shown that the first term in (90) is bounded from below by

$$f(\lambda_{\max},\lambda_{\min})=\frac{\mu}{J_e^{2/3}}\Big[1-\frac{4}{3}\frac{\lambda_{\max}}{\lambda_{\min}}+\frac{5}{9}\frac{1}{\lambda_{\max}^2}(\lambda_{\max}^2+\lambda_{\min}^2)\Big]. \tag{91}$$

The sign of the function (91) is plotted in Fig. 12. It is noted that a minimal range of elastic deformations in which the function is positive is $0.85<\lambda_{\min}\leq\lambda_{\max}<1.15$, denoted by the triangular region in the figure. This range is sufficiently large to ensure strong ellipticity of the free energy function for all practical applications involving compaction of granular materials.

C Augmented primal closest-point projection

The augmented primal closest-point projection method proposed in [23] has proven to significantly improve the convergence of the Newton method used for the solution of the return-mapping equations in the constitutive update problem defined in Section 4.3. The idea is to apply the augmented Lagrangian method to enforce the inequality constraints corresponding to the incremental complementarity conditions, cf. Eq. (51),

$$F^*_{n+1}\leq 0,\qquad\Delta\lambda\geq 0,\qquad\Delta\lambda F^*_{n+1}=0. \tag{92}$$

The simple treatment proposed in [23] amounts to replacing the plastic multiplier $\Delta\lambda$ in the incremental flow rule (50) by the augmented one, $\Delta\hat{\lambda}$,

$$\Delta\hat{\lambda}=\max(0,\Delta\lambda+\rho F^*_{n+1}), \tag{93}$$

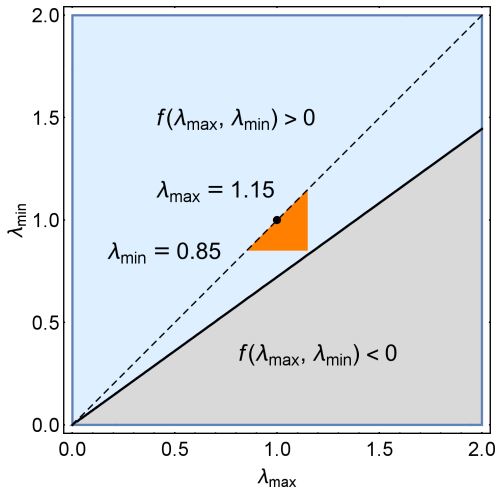

Figure 12: Sign of the function $f(\lambda_{\max}, \lambda_{\min})$, which is a lower bound for the positive definiteness of the acoustic tensor (89). The triangular region denotes the range $0.85 < \lambda_{\min} \leq \lambda_{\max} < 1.15$ in which the acoustic tensor is clearly positive definite and therefore strong ellipticity is ensured.

where $\rho > 0$. The condition $F^*_{n+1} = 0$ is modified accordingly,

$$\hat{F}^*_{n+1} = \frac{1}{\rho}(\Delta\hat{\lambda} - \Delta\lambda) = 0, \tag{94}$$

which now enforces $F^*_{n+1} = 0$ when $\Delta\lambda + \rho F^*_{n+1} > 0$ and $\Delta\lambda = 0$ otherwise. As a result, the local residual $\mathbf{Q}_{n+1}$ is redefined as

$$\mathbf{Q}_{n+1} = \{\mathcal{Z}_{11}, \mathcal{Z}_{22}, \mathcal{Z}_{33}, \mathcal{Z}_{12}, \mathcal{Z}_{13}, \mathcal{Z}_{23}, \hat{F}^*_{n+1}, \mathcal{A}\}, \tag{95}$$

with $\mathcal{Z}_{ij}$ given by

$$\mathcal{Z}_{ij} = \left(\boldsymbol{T}^{(2)}_{n+1} - \boldsymbol{T}^{(2)}_{n} - \mathbb{E}_{n+1}[\boldsymbol{E}^{(2)}_{n+1} - \boldsymbol{E}^{(2)}_{n} - \Delta\hat{\lambda}\hat{\boldsymbol{N}}^*_{n+1}] \right)_{ij}. \tag{96}$$

Note that the converged solution of the return mapping algorithm is not affected by the above treatment and does not depend on the value of parameter ρ.

Although the solution sought in the plastic state ($F^{*trial}_{n+1} > 0$) corresponds to a strictly positive $\Delta\lambda$, the above simple treatment leads to a significant increase of the radius of convergence of the Newton method (actually, now a semi-smooth Newton method due to the $\max(\cdot)$ function in the definition of $\Delta\hat{\lambda}$) so that the computations may proceed with larger time increments.

Actually, for compaction by a cross-shaped punch, the classical return mapping algorithm did not converge at the initial stage of the process so that the corresponding simulation could not be completed. At the same time, the enhanced algorithm performs very well, as illustrated in Fig. 8.

The convergence behaviour of the enhanced algorithm does depend on the value of parameter ρ, although the solution, if achieved, does not. This is illustrated in Fig. 13 which shows the number of time steps needed to complete the simulation (using an adaptive time incrementation scheme) as a function of parameter ρ. Considering that the

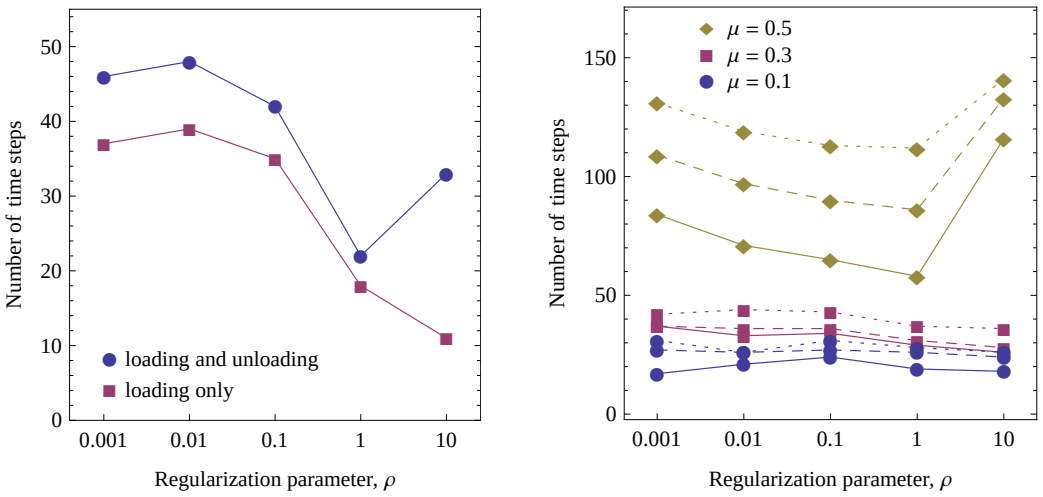

Figure 13: Number of time steps as a function of parameter ρ for: (a) compaction by a cross-shaped punch, (b) compaction in a cylindrical die with die-wall friction (solid lines correspond to the initial aspect ratio $h_0/r = 2$, dashed lines to $h_0/r = 4$, and dotted lines to $h_0/r = 6$).

material response and the tangent operator are not affected by the value of ρ, the achievable time increment size is constrained by the radius of convergence of the return mapping algorithm. It follows from Fig. 13 that $\rho = 1$ seems to be an optimal value in the present application (the result reported in Fig. 8 corresponds to $\rho = 1$). However, it is seen that the enhanced algorithm performs correctly for a wide range of values of ρ.

It is also seen that combination of elastoplastic material behaviour and frictional contact, as in the analysis of axisymmetric compaction in Section 5.2, may adversely affect the overall convergence behaviour which is due to additional nonlinearities introduced by contact and friction, particularly for high friction coefficient $\mu = 0.5$, see Fig. 13b.

Finally, as shown in Fig. 14, the enhanced algorithm with the optimal value of $\rho = 1$ performs significantly better than the classical return mapping algorithm. For other values of ρ, the difference is somewhat less pronounced, but the enhanced algorithm is still beneficial.

References

[1] J. C. Simo and T. J. R. Hughes. *Computational Inelasticity*. Springer-Verlag, New York, 1998.

[2] E. A. de Souza Neto, D. Peric, and D. R. J. Owen. *Computational Methods for Plasticity: Theory and Applications*. Wiley, 2008.

[3] R. I. Borja and C. Tamagnini. Cam-Clay plasticity Part III: Extension of the infinitesimal model to include finite strains. *Comp. Meth. Appl. Mech. Engng.*, 155:73–95, 1998.

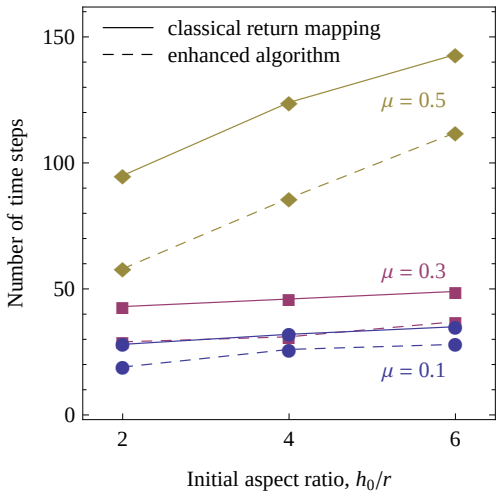

Figure 14: Compaction in a cylindrical die: number of time steps as a function of parameter ρ. Solid lines correspond to the classical return mapping algorithm and dashed lines to the augmented algorithm with $\rho = 1$.

[4] G. Meschke and W. N. Liu. A re-formulation of the exponential algorithm for finite strain plasticity in terms of Cauchy stresses. *Comp. Meth. Appl. Mech. Engng.*, 173:167–187, 1999.

[5] A. Perez-Foguet, A. Rodriguez-Ferran, and A. Huerta. Efficient and accurate approach for powder compaction problems. *Comp. Mech.*, 30:220–234, 2003.

[6] M. Ortiz and A. Pandolfi. A variational Cam-clay theory of plasticity. *Comp. Meth. Appl. Mech. Engng.*, 193:27–29, 2004.

[7] M. Rouainia and D. M. Wood. Computational aspects in finite strain plasticity analysis of geotechnical materials. *Mech. Res. Comm.*, 33:123–133, 2006.

[8] G. Frenning. Analysis of pharmaceutical powder compaction using multiplicative hyperelasto-plastic theory. *Powder Technol.*, 172:103–112, 2007.

[9] A. Karrech, K. Regenauer-Lieb, and T. Poulet. Frame indifferent elastoplasticity of frictional materials at finite strain. *Int. J. Sol. Struct.*, 48:397–407, 2011.

[10] A. Piccolroaz, D. Bigoni, and A. Gajo. An elastoplastic framework for granular materials becoming cohesive through mechanical densification. Part I – small strain formulation. *Eur. J. Mech. A/Solids*, 25:334–357, 2006.

[11] A. Piccolroaz, D. Bigoni, and A. Gajo. An elastoplastic framework for granular materials becoming cohesive through mechanical densification. Part II – the formulation of elastoplastic coupling at large strain. *Eur. J. Mech. A/Solids*, 25:358–369, 2006.

[12] D. Bigoni and A. Piccolroaz. Yield criteria for quasibrittle and frictional materials. *Int. J. Sol. Struct.*, 41:2855–2878, 2004.

[13] J. Korelc. Multi-language and multi-environment generation of nonlinear finite element codes. *Engineering with Computers*, 18:312–327, 2002.

[14] J. Korelc. Automation of primal and sensitivity analysis of transient coupled problems. *Comp. Mech.*, 44:631–649, 2009.

[15] S. Stupkiewicz, A. Piccolroaz, and D. Bigoni. Elastoplastic coupling to model cold ceramic powder compaction. *J. Eur. Cer. Soc.*, 34:2839–2848, 2014.

[16] D. Bigoni. Bifurcation and instability of non-associative elastoplastic solids. In H. Petryk, editor, *Material Instabilities in Elastic and Plastic Solids*, volume 414 of *CISM Courses and Lectures*, pages 1–52. Springer-Verlag Wien, 2000.

[17] S. Stupkiewicz, R. Denzer, A. Piccolroaz, and D. Bigoni. Implicit yield function formulation for granular and rock-like materials. *Comp. Mech.*, 54:1163–1173, 2014.

[18] R. Hill and J. R. Rice. Elastic potentials and the structure of inelastic constitutive laws. *SIAM J. Appl. Math.*, 25:448–461, 1973.

[19] R. M. Brannon and S. Leelavanichkul. A multi-stage return algorithm for solving the classical damage component of constitutive models for rocks, ceramics, and other rock-like media. *Int. J. Fract.*, 163:133–149, 2010.

[20] M. Penasa, A. Piccolroaz, L. Argani, and D. Bigoni. Integration algorithms of elastoplasticity for ceramic powder compaction. *J. Eur. Cer. Soc.*, 34:2775–2788, 2014.

[21] G. Weber and L. Anand. Finite deformation constitutive equations and a time integration procedure for isotropic, hyperelastic–viscoplastic solids. *Comp. Meth. Appl. Mech. Engng.*, 79:173–202, 1990.

[22] P. Steinmann and E. Stein. On the numerical treatment and analysis of finite deformation ductile single crystal plasticity. *Comp. Meth. Appl. Mech. Engng.*, 129:235–254, 1996.

[23] A. Perez-Foguet and F. Armero. On the formulation of the closest-point projection algorithms in elastoplasticity—part II: Globally convergent schemes. *Int. J. Num. Meth. Engng.*, 53:331–374, 2002.

[24] J. Korelc and S. Stupkiewicz. Closed-form matrix exponential and its application in finite-strain plasticity. *Int. J. Num. Meth. Engng.*, 98:960–987, 2014.

[25] P. Michaleris, D. A. Tortorelli, and C. A. Vidal. Tangent operators and design sensitivity formulations for transient non-linear coupled problems with applications to elastoplasticity. *Int. J. Num. Meth. Engng.*, 37:2471–2499, 1994.

[26] E. A. de Souza Neto, D. Perić, M. Dutko, and D. R. J. Owen. Design of simple low order finite elements for large strain analysis of nearly incompressible solids. *Int. J. Sol. Struct.*, 33:3277–3296, 1996.

[27] J. Korelc and P. Wriggers. Improved enhanced strain four-node element with Taylor expansion of the shape functions. *Int. J. Num. Meth. Engng.*, 40:407–421, 1997.

[28] P. Alart and A. Curnier. A mixed formulation for frictional contact problems prone to Newton like solution methods. *Comp. Meth. Appl. Mech. Engng.*, 92:353–375, 1991.

[29] J. Lengiewicz, J. Korelc, and S. Stupkiewicz. Automation of finite element formulations for large deformation contact problems. *Int. J. Num. Meth. Engng.*, 85:1252–1279, 2011.

[30] Z. P. Bazant. Easy-to-compute tensors with symmetric inverse approximating Hencky finite strain and its rate. *Trans. ASME J. Eng. Mat. Technol.*, 120:131–136, 1998.

[31] R. Hill. On constitutive inequalities for simple materials – I. *J. Mech. Phys. Solids*, 16:229–242, 1968.